

Cosmic rays and the magnetic field in the nearby starburst galaxy NGC 253

II. The magnetic field structure[★]

V. Heesen^{1,3}, M. Krause², R. Beck², and R.-J. Dettmar³

¹ Centre for Astrophysics Research, University of Hertfordshire, Hatfield AL10 9AB, UK
e-mail: v.heesen@herts.ac.uk

² Max-Planck-Institut für Radioastronomie, Auf dem Hügel 69, 53121 Bonn, Germany

³ Astronomisches Institut der Ruhr-Universität Bochum, Universitätsstr. 150, 44780 Bochum, Germany

Received 21 January 2009 / Accepted 29 July 2009

ABSTRACT

Context. There are several edge-on galaxies with a known magnetic field structure in their halo. A vertical magnetic field significantly enhances the cosmic-ray transport from the disk into the halo. This could explain the existence of the observed radio halos.

Aims. We observed NGC 253 that possesses one of the brightest radio halos discovered so far. Since this galaxy is not exactly edge-on ($i = 78^\circ$) the disk magnetic field has to be modeled and subtracted from the observations in order to study the magnetic field in the halo.

Methods. We used radio continuum polarimetry with the VLA in D-configuration and the Effelsberg 100-m telescope. NGC 253 has a very bright nuclear point-like source, so that we had to correct for instrumental polarization. We used appropriate Effelsberg beam patterns and developed a tailored polarization calibration to cope with the off-axis location of the nucleus in the VLA primary beams. Observations at $\lambda\lambda 6.2$ cm and 3.6 cm were combined to calculate the RM distribution and to correct for Faraday rotation.

Results. The large-scale magnetic field consists of a *disk* (r, ϕ) and a *halo* (r, z) component. The disk component can be described as an axisymmetric spiral field pointing inwards with a pitch angle of $25^\circ \pm 5^\circ$ which is *symmetric* with respect to the plane (even parity). This field dominates in the disk, so that the observed magnetic field orientation is disk parallel at small distances from the midplane. The halo field shows a prominent X-shape centered on the nucleus similar to that of other edge-on galaxies. We propose a model where the halo field lines are along a cone with an opening angle of $90^\circ \pm 30^\circ$ and are pointing away from the disk in both the northern and southern halo (even parity). We can not exclude that the field points inwards in the northern halo (odd parity). The X-shaped halo field follows the lobes seen in $H\alpha$ and soft X-ray emission.

Conclusions. Dynamo action and a disk wind can explain the X-shaped halo field. The nuclear starburst-driven superwind may further amplify and align the halo field by compression of the lobes of the expanding superbubbles. The disk wind is a promising candidate for the origin of the gas in the halo and for the expulsion of small-scale helical fields as requested for efficient dynamo action.

Key words. galaxies: individual: NGC 253 – magnetic fields – methods: observational – methods: data analysis – galaxies: halos – galaxies: ISM

1. Introduction

There is increasing observational evidence for the existence of gaseous halos around disk galaxies. They consist of different interstellar medium (ISM) species, mainly the diffuse ionized gas, dust, cosmic rays (CRs), and magnetic fields (for a review, see e.g. Dettmar 1992). The transport of gas from the disk into the halo has been discussed in the past in terms of galactic chimneys (Norman & Ikeuchi 1989) and superbubble blow outs (Mac Low & Ferrara 1999). These models all include supernova explosions as the energy source that drives the formation of the halo. The effects of star formation on the ISM are dramatic: the heated gas in supernova remnants and accelerated energetic particles are injected into the base of the halo. The fundamental parameter, which determines the formation of a halo, is therefore the energy input by supernova explosions. Thus, the halo does not form above the entire disk, but only at radial distances where the

star formation takes place (Dahlem et al. 1995). Moreover, the compactness of the star-forming regions determines the threshold condition where the hot gas can break out against the pull of the gravitational field (Dahlem et al. 2006). This corroborates the picture of the hot gas injected by supernova explosions and stellar winds of massive stars (see e.g. Dettmar & Soida 2006).

Direct evidence for supernova-heated galactic halos comes from imaging and spectroscopy of diffuse soft X-ray emission. This has been impressively demonstrated by XMM-Newton observations of NGC 253 where the nuclear X-ray plume can be explained only by star formation without the contribution of an AGN (Pietsch et al. 2001; Bauer et al. 2008). Moreover, it clearly shows that the galactic starburst must drive a thermal outflow, since there are strong indications of collisionally excited oxygen and iron L line complexes in the spectrum (Breitschwerdt 2003).

In a pioneering work Ipavich (1975) pointed out the importance of CRs for the generation of a galactic wind. In the disk, the CR gas, the magnetic field, and the hot gas contribute roughly the same amount of pressure (Beck et al. 1996). In the halo,

[★] Appendix is only available in electronic form at <http://www.aanda.org>

however, CRs and the magnetic field dominate. The relativistic CR gas has a larger pressure scaleheight than the hot gas, because its adiabatic index is $4/3$ whereas it is $5/3$ for the hot gas; the magnetic field has an even larger scaleheight (Beck 2007). Furthermore, the CR nucleons, which contain the bulk of the energy, do not suffer from strong radiative losses like the hot gas. The CR-driven galactic wind is thus another scenario which needs consideration when discussing gaseous halos.

The theoretical framework for the CR transport is given by the combined diffusion-convection equation, which can be applied in the local comoving coordinate system if the bulk speed of the background medium is non-relativistic (Schlickeiser 2002). Breitschwerdt et al. (1991, 1993) applied the transport equation for different magnetic field configurations in the Milky Way. They concluded that the CR transport can be split in an *entirely diffusive* and an *entirely convective* regime, depending only on the local magnetic field configuration. For the lower Milky Way halo they assumed the magnetic field lines to be turbulently excited by stochastic gas motions caused by expanding and overlapping supernova remnants. Thus, there will be no preferred direction of propagation of these magnetic fluctuations and hence no net Alfvénic drift. In the halo the magnetic field lines of the superbubbles begin to overlap and form “open” field lines that might be enhanced by magnetic reconnection (Parker 1992).

Various polarization studies have shown that magnetic fields are a very sensitive tracer of interaction in the ISM that is not visible at any other wavelength. Chyży & Beck (2004) showed that the interacting pair of galaxies NGC 4038/39 (the Antennae) possesses a strong magnetic field of $20 \mu\text{G}$, significantly stronger than non-interacting spirals. The polarized emission in many of the Virgo cluster galaxies is shifted with respect to the optical distribution (Weżgowiec et al. 2007). Simulations suggest that this behavior can be explained by ram pressure stripping of galaxies moving through the intracluster medium (Soida et al. 2006; Vollmer et al. 2008). But a close inspection of the Virgo spiral NGC 4254 showed that the observed magnetic field structure requires additional MHD mechanisms other than ram pressure stripping (Chyży et al. 2007; Chyży 2008). The structure of the magnetic field is thus an important tracer for MHD processes and the interaction between various ISM components, which are expected to be present in galaxies with winds.

From these considerations it is clear that there is a need for understanding the three-dimensional structure of the magnetic field in the halo of spiral galaxies. That restricts the observations to a few nearby edge-on galaxies that allow us to study the extraplanar magnetic field with high spatial resolution and sensitivity. Several edge-on galaxies have a known magnetic field structure (Golla & Hummel 1994; Dumke & Krause 1998; Tüllmann et al. 2000; Krause 2004; Dettmar & Soida 2006; Krause 2009). The nearby starburst galaxy NGC 253 possesses one of the brightest radio halos discovered so far, but the inclination angle is only mildly edge-on ($i = 78.5^\circ$). We assumed a distance of 3.94 Mpc (Karachentsev et al. 2003) where an angular resolution of $30''$ corresponds to a spatial resolution of 600 pc. Furthermore, we used $P.A. = 52^\circ$ as the position angle of the major axis.

This paper is the successive paper of Heesen et al. (2009) (Paper I thereafter) where the CR distribution in NGC 253 was found to be consistent with a vertical CR transport from the disk into the halo. In contradiction to this finding so far no vertical magnetic field has been discovered in the halo of this galaxy. The most detailed discussion of the magnetic field structure was presented by Beck et al. (1994), where a mainly disk-parallel magnetic field was found in the disk and halo. This was explained by a strong shearing of the magnetic field due to differential

rotation. The study presented in the present paper provides new sensitive observations of the large-scale magnetic field in the halo of NGC 253. We use the polarimetry information of the observations presented in Paper I at different wavelengths which allow us to apply a correction for the Faraday rotation and thus to determine the intrinsic magnetic field orientation.

This paper is organized as follows: we start with the description of the observations and explain especially the calibration of the polarization in order to cope with instrumental polarization caused by the high dynamic range (Sect. 2). We present the continuum maps of NGC 253 along with the vectors of the intrinsic magnetic field and briefly describe its morphology in Sect. 3. Section 4 summarizes the polarization properties. In Sect. 5 we investigate the magnetic field structure and present a model for the large-scale magnetic field. In Sect. 6 we discuss the consequences of our findings for the radio halo of NGC 253 and the observed other phases of the ISM. Finally we summarize our results and present the conclusions in Sect. 7.

2. Observations and data reduction

2.1. Effelsberg observations

In Paper I we described our radio continuum observations of NGC 253 at $\lambda 6.2$ cm and 3.6 cm with the 100-m Effelsberg telescope¹. Here we only explain the details important for the polarization measurements and for the general calibration and data reduction we refer to Paper I. The high dynamic range (≥ 1000) due to the strong nuclear point-like source (hereafter for simplicity called the nucleus) requires several additional steps in the data reduction. In Paper I we explained how we removed the sidelobes of the nucleus via a Högbom cleaning of the total power maps. But the high dynamic range also influences the polarization via the leakage of total power emission to the polarized intensity. The flux density of the so-called *instrumental polarization* is about 1.0% for the Effelsberg telescope with respect to the total power flux density (Heesen 2008). Thus, it can be neglected only for observations with a dynamic range significantly less than 100 which is not fulfilled for our observations.

In order to apply a correction for the instrumental polarization we used beam patterns for Stokes parameters Q and U obtained from deep observations of the unpolarized point-like source 3C84. The cleaned total power emission was convolved with the beam patterns and the computed instrumental contribution was subtracted from the Stokes Q and U maps, respectively. Finally we obtained the map of the polarized intensity from the corrected Stokes Q and U maps using COMB (part of AIPS)². We applied a correction for the noise bias in order to preserve the mean zero level of the polarized intensity. The rms noise levels of the final maps are $200 \mu\text{Jy}/\text{beam}$ for $\lambda 6.2$ cm at $144''$ resolution and $100 \mu\text{Jy}/\text{beam}$ for $\lambda 3.6$ cm at $84''$ resolution, respectively³.

2.2. VLA observations

For the polarization calibration of the VLA mosaic at $\lambda 6.2$ cm (see Paper I) we met the challenge that the nucleus is located

¹ The Effelsberg 100-m telescope is operated by the Max-Planck-Institut für Radioastronomie (MPIfR).

² The Astronomical Image Processing System (AIPS) is distributed by the National Radio Astronomy Observatory (NRAO) as free software.

³ All angular resolutions in this paper are referred to as the half power beam width (HPBW).

at the edge of the primary beam in some of our pointings⁴. In the center of the primary beam the instrumental polarization is less than 0.1% but at the edge of the primary beam it rises to more than 1%. The variability in time due to the apparent circular motion of the nucleus around the center in the primary beam, caused by the alt-azimuthal mount of the VLA antennas, complicates the situation even further. This prevents the removal of sidelobes with the Högbom clean algorithm as it works only for non-variable sources. Thus, the standard polarization calibration technique applied in case of NGC 253 leads to a polarization map completely dominated by instrumental polarization.

Hence, we developed a specially tailored technique for the pointings with the nucleus located at the edge of the primary beam. The polarization calibration PCAL (part of AIPS) was applied to the nucleus itself instead of the secondary (phase) calibrator in order to find a solution for the off-axis instrumental polarization. The appropriate beam patterns in Stokes Q and U allowed us to subtract the nucleus from the (u, v) -data of individual “snapshots”, which contained less than 10 min of observing time. This effectively removes the time-variable contribution of the instrumental polarization caused by the nucleus. Thus we were able to use the full set of (u, v) -data in order to get the best (u, v) -coverage which resulted in the expected sensitivity of the extended emission. A more detailed description of the polarization calibration can be found in Heesen (2008).

The pointings that are not influenced by the nucleus were calibrated in the standard way with the secondary calibrator using PCAL. Inverting the (u, v) -data with natural weighting (i.e. Briggs Robust = 8) we produced maps of all pointings in Stokes Q and U , which were convolved with a Gaussian to 30'' resolution. The combination of the pointings was done with LTESS (part of AIPS) which performs a linear superposition with a correction for the VLA primary beam attenuation using information from each pointing out to the 7% level of the primary beam (Braun 1988). The final maps are essentially noise limited with a sensitivity of 30 $\mu\text{Jy}/\text{beam}$ at 30'' resolution in Stokes Q and U . We used IMERG (part of AIPS) for the combination of the VLA and Effelsberg Stokes Q and U maps in order to fill in the missing zero-spacing flux; this was done for the total power (Stokes I) map also. The map of the polarized intensity was computed again using POLC with a correction for the noise bias.

3. Morphology of the polarized emission

In this section we discuss the morphology of the polarized emission and the magnetic field orientation. In the figures, the first contours indicate emission at three times the (apparent) rms noise level ($2^{m-1} \times 3 \text{ rms}$; $m = 1, 2, 3, \dots$). The polarization vectors (E -vectors) were rotated by 90° in order to display the orientation of the magnetic field vectors (B -vectors). We have clipped the vectors below two times the rms noise level in polarized intensity. The optical background image in Figs. 1–3 is from the DSS (when the radio continuum map is smaller than the background image, its boundary is indicated by dashed lines)⁵. A summary of the polarization observations presented in this paper is given in Table 1.

⁴ The VLA (Very Large Array) is operated by the NRAO (National Radio Astronomy Observatory).

⁵ The compressed files of the “Palomar Observatory – Space Telescope Science Institute Digital Sky Survey” (DSS) of the northern sky, based on scans of the Second Palomar Sky Survey are ©1993–1995 by the

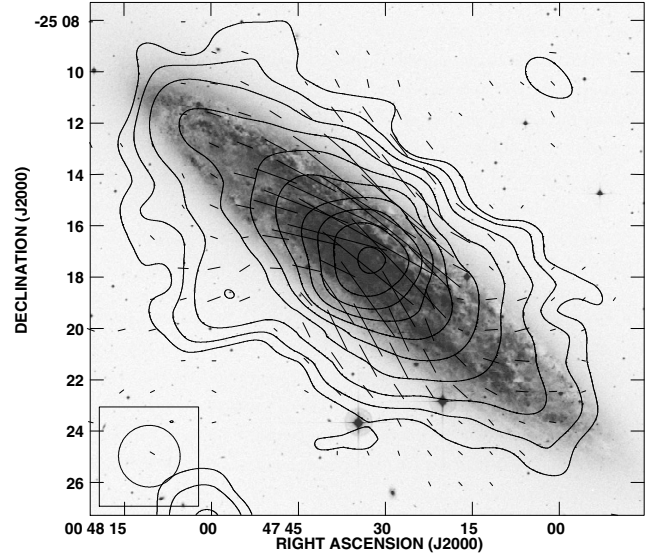


Fig. 1. Total power radio continuum at $\lambda 6.2$ cm from Effelsberg observations with 144'' resolution. Contours are at 3, 6, 12, 24, 48, 96, 192, 384, 768, and 1536×1 mJy/beam (the rms noise level). The vectors show the orientation of the large-scale magnetic field (not corrected for Faraday rotation). A vector length of 1'' is equivalent to 50 $\mu\text{Jy}/\text{beam}$ polarized intensity. The circle in the lower left corner in this and the following figures indicates the size of the beam.

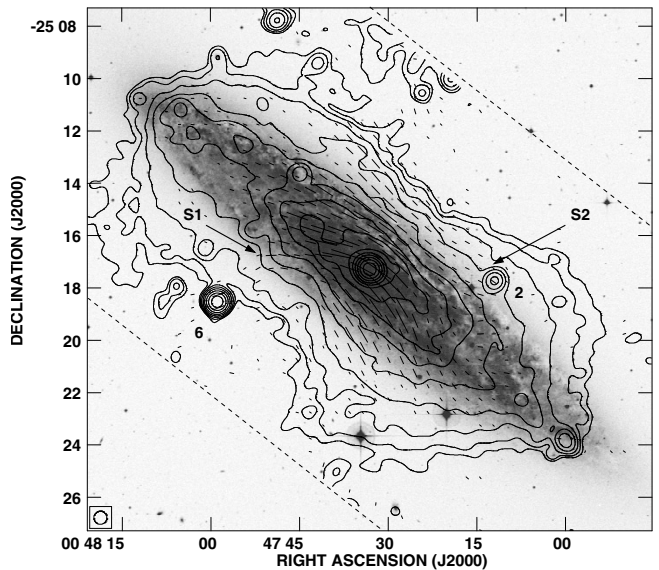


Fig. 2. Total power radio continuum at $\lambda 6.2$ cm from combined VLA + Effelsberg observations with 30'' resolution. Contours are at 3, 6, 12, 24, 48, 96, 192, 384, 768, 1536, 3077, 6144, 12288, and 24576×30 $\mu\text{Jy}/\text{beam}$ (the rms noise level). The vectors show the orientation of the large-scale magnetic field (not corrected for Faraday rotation). A vector length of 1'' is equivalent to 12.5 $\mu\text{Jy}/\text{beam}$ polarized intensity. The spurs S1 and S2 and the point-like sources no. 2 and no. 6 are indicated.

In Fig. 1 we present the distribution of the total power radio continuum emission together with the B -vectors from the $\lambda 6.2$ cm Effelsberg observations. The low resolution of 144'' shows the magnetic field structure at the largest scales. The magnetic field is disk parallel only in the disk plane. Further away

California Institute of Technology and are distributed herein by agreement.

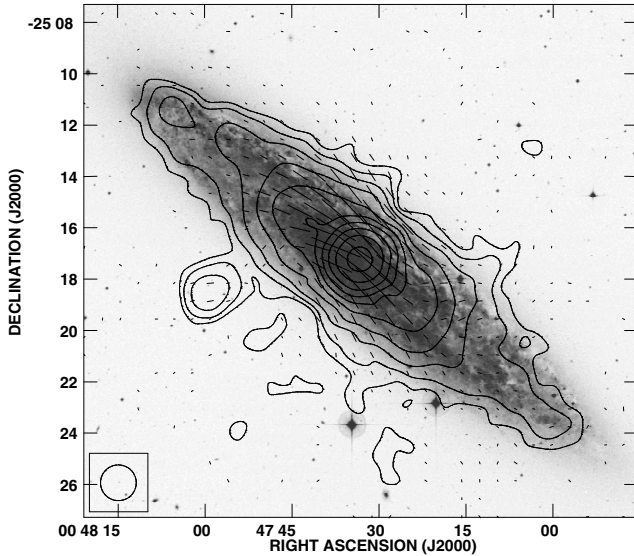


Fig. 3. Total power radio continuum at $\lambda 3.6$ cm from Effelsberg observations with $84''$ resolution. Contours are at 3, 6, 12, 24, 48, 96, 192, 384, 768, and $1536 \times 500 \mu\text{Jy}/\text{beam}$ (the rms noise level). The vectors show the orientation of the large-scale magnetic field (not corrected for Faraday rotation). A vector length of $1''$ is equivalent to $50 \mu\text{Jy}/\text{beam}$ polarized intensity.

Table 1. Maps of NGC 253 presented in this paper of total power radio continuum (TP) and polarized intensity (PI).

| λ [cm] | Telescope | Resolution | TP rms [mJy/beam] | PI rms [mJy/beam] |
|-------------------|------------------|------------|----------------------|----------------------|
| 6.2 | VLA + Effelsberg | $30''$ | 0.03 | 0.03 |
| 6.2 | Effelsberg | $144''$ | 1.00 | 0.20 |
| 3.6 | Effelsberg | $84''$ | 0.50 | 0.10 |

from the disk, it has a significant vertical component. From the combined VLA + Effelsberg observations at $\lambda 6.2$ cm we created the map shown in Fig. 2 with $30''$ resolution. At the location S1 the magnetic field orientation is almost perpendicular to the disk. This is an example of a “radio spur” where the large-scale magnetic field opens from a disk parallel to a vertical field. At its end away from the disk the point-like source no. 6 is located; this polarized source likely is a background AGN (Carilli et al. 1992). The second radio spur S2 has a magnetic field orientation of 45° with respect to the major axis; the unpolarized point-like source no. 2 is located at its end away from the disk.

We show the $\lambda 3.6$ cm Effelsberg map in Fig. 3. At a resolution of $84''$ this map reveals no new details. But it is important for the determination of the Faraday rotation as shown in Sect. 4.2.

The distribution of the polarized intensity from the $\lambda 6.2$ cm Effelsberg observations is presented in Fig. 4. It is very different from the total power distribution that can be described by a thick radio disk with a vertical exponential profile. Figure 4 shows a thick disk formed by extensions E1 and E2, apparent in the VLA + Effelsberg map (Fig. 5).

Figure 5 shows the distribution of the polarized intensity from the combined $\lambda 6.2$ cm VLA + Effelsberg observations. The bulk of the polarized emission arises in the disk and extends into the halo. In contrast, in the outer parts of the disk the polarized emission is weak at this resolution. The polarized emission extends to large vertical heights above the inner disk.

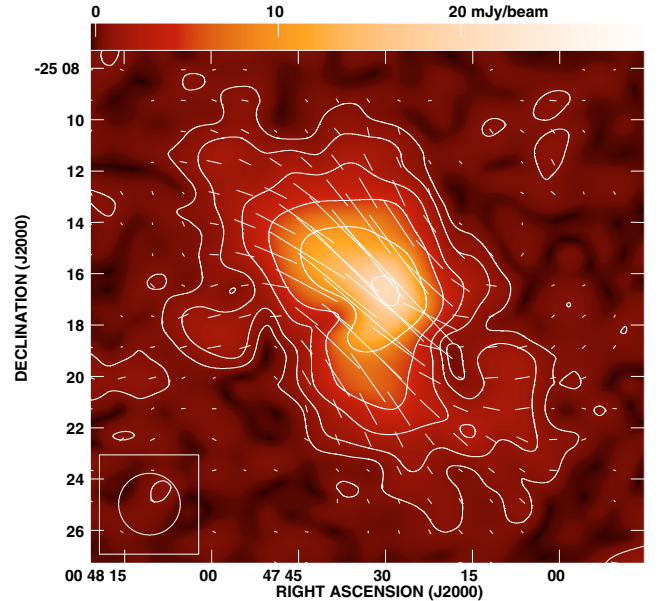


Fig. 4. Polarized intensity at $\lambda 6.2$ cm from Effelsberg observations with $144''$ resolution. Contours are at 3, 6, 12, 24, 48, and 96 times $200 \mu\text{Jy}/\text{beam}$ (the rms noise level). The vectors show the orientation of the Faraday corrected large-scale magnetic field. A vector length of $1''$ is equivalent to $50 \mu\text{Jy}/\text{beam}$ polarized intensity.

The Effelsberg $\lambda 3.6$ cm map of the polarized intensity presented in Fig. 6 is similar to Fig. 5 where the emission is slightly more concentrated to the disk than at $\lambda 6.2$ cm. This can be explained by the smaller scaleheight of the total power emission at this shorter wavelength due to higher synchrotron losses that influence also the polarized emission (see Paper I).

The polarized intensity has a minimum between the radio spur S1 and the extension E2. Another minimum of polarized intensity is located near the radio spur S2. We will refer to these regions as “depolarized regions”. The large-scale magnetic field is disk parallel near the galactic midplane whereas at some locations we find a significant vertical component. Hence, the large-scale magnetic field may consist of two components, one disk parallel and one vertical.

4. Polarization properties

4.1. Degree of polarization

Linearly polarized synchrotron emission is observed from CR electrons spiraling in an ordered magnetic field. No linearly polarized signal is detected from isotropic turbulent magnetic fields with randomly distributed directions⁶. Hence, we can use the polarization degree as a measure of the ratio between the ordered and the turbulent magnetic field.

The integrated polarized flux densities were obtained by integration in ellipses which include the extra-planar emission as described in Paper I (see Table 2). The error of the flux densities was calculated as the quadratic sum of a 5% calibration error

⁶ Note that the observed B -vectors of linearly polarized emission can trace either *regular* magnetic fields (i.e. preserving their direction within the telescope beam) or *anisotropic* fields (i.e. with multiple field reversals within the beam). Anisotropic fields can be generated from turbulent fields by shear or winds. To distinguish between these two components, additional Faraday rotation data is needed. The fields observed in polarization are called “ordered” throughout this paper.

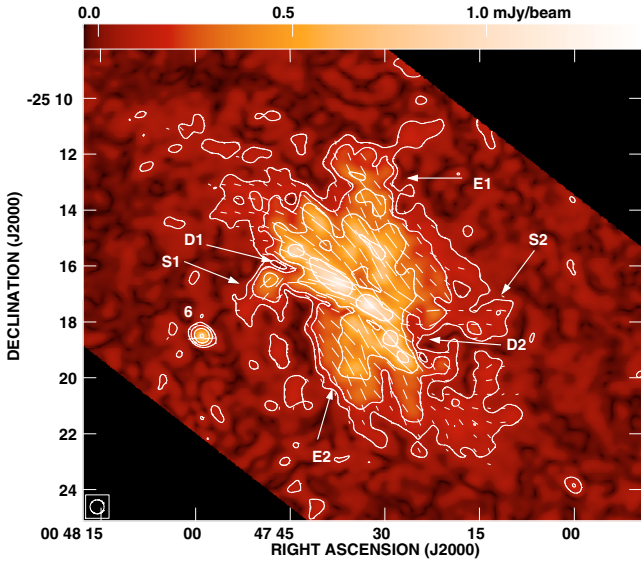


Fig. 5. Polarized intensity at $\lambda 6.2$ cm from combined VLA + Effelsberg observations with $30''$ resolution. Contours are at $3, 6, 12,$ and $24 \times 30 \mu\text{Jy}/\text{beam}$ (the rms noise level). The vectors show the Faraday corrected orientation of the large-scale magnetic field. A vector length of $1''$ is equivalent to $12.5 \mu\text{Jy}/\text{beam}$ polarized intensity. The extensions E1 and E2, the spurs S1 and S2, the relative minima D1 and D2, and the point-like source no. 6 are indicated.

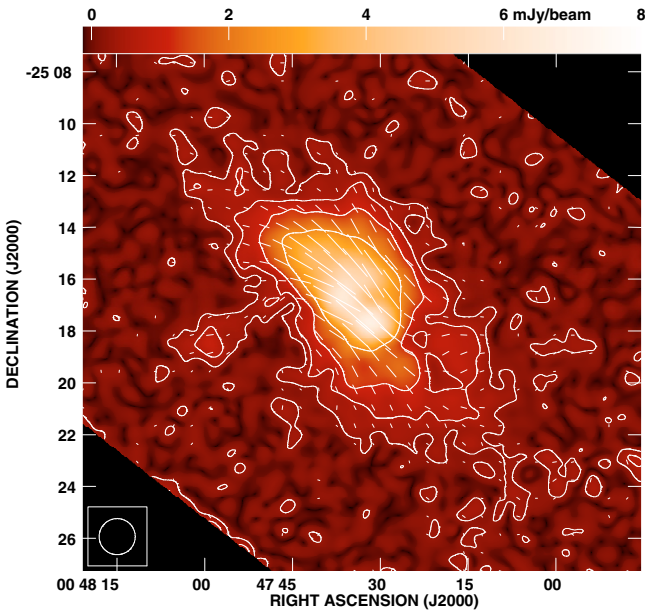


Fig. 6. Polarized intensity at $\lambda 3.6$ cm from Effelsberg observations with $84''$ resolution. Contours are at $3, 6, 12,$ and $24 \times 100 \mu\text{Jy}/\text{beam}$ (the rms noise level). The vectors show the Faraday corrected orientation of the large-scale magnetic field. A vector length of $1''$ is equivalent to $50 \mu\text{Jy}/\text{beam}$ polarized intensity.

and the baselevel error. The polarization degree P is the ratio of the flux density of the extended total power emission S_e (nucleus subtracted) to that of the polarized emission S_p . The polarization degree is between 6% and 9%, which is similar to values found in other galaxies.

In Fig. 7 we present the distribution of the degree of polarization at $\lambda 6.2$ cm. It has a minimum in the midplane where it is smaller than 10%. Values larger than 20% are found at the radio

Table 2. Integrated flux densities.

| λ [cm] | Instrument | S_e [mJy] | S_p [mJy] | P [%] |
|----------------|------------|---------------|-------------|---------------|
| 6.2 | VLA + Eff. | 1440 ± 70 | 80 ± 12 | 5.6 ± 1.1 |
| 6.2 | VLA | 1160 ± 60 | 64 ± 12 | 5.5 ± 1.3 |
| 6.2 | Effelsberg | 1430 ± 70 | 87 ± 18 | 6.1 ± 1.6 |
| 3.6 | Effelsberg | 680 ± 40 | 60 ± 10 | 8.8 ± 2.0 |

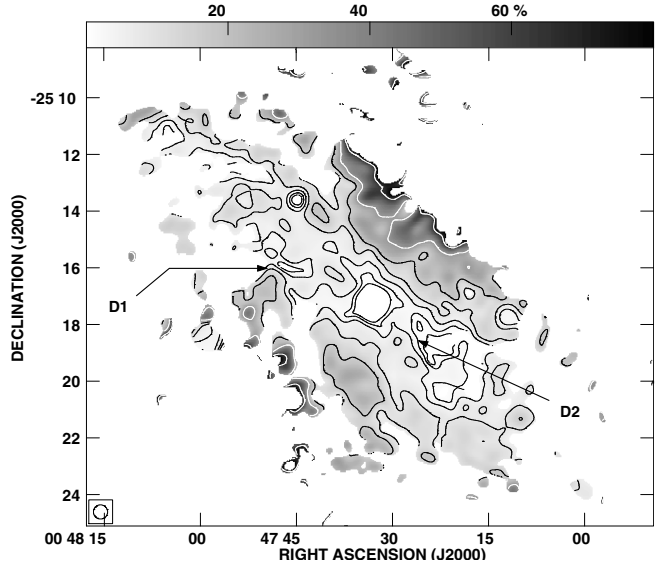


Fig. 7. Degree of polarization at $\lambda 6.2$ cm from combined VLA + Effelsberg observations with $30''$ resolution. Contours are at $1, 2, 4, 8, 16, 32,$ and $64 \times 1\%$. The depolarized regions D1 and D2 are indicated.

spur S1 and at the extensions E1 and E2. The depolarized regions D1 and D2 are prominently visible as local minima.

4.2. Distribution of the rotation measure

The polarization angle of the magnetic field vectors is changed by the Faraday rotation which depends on the square of the wavelength. If the Faraday depolarization is small, we can calculate the rotation measure (RM) from the rotation $\Delta\chi$ of the polarization vector between two wavelengths:

$$\Delta\chi = \text{RM} \cdot (\lambda_1^2 - \lambda_2^2). \quad (1)$$

In Fig. 8 we present the RM distribution between $\lambda 6.2$ cm and 3.6 cm at $144''$ resolution. We see a gradual change of positive RMs in the northeastern half of the galaxy to negative RMs in the southwestern half. Strong negative RMs ($< -200 \text{ rad m}^{-2}$) in region D2 are an artifact due to strong Faraday depolarization (Sokoloff et al. 1998).

According to the RM distribution the large-scale magnetic field has a line-of-sight component that is pointing to the observer in the northeastern half and pointing away from the observer in the southwestern half. This agrees with a spiral magnetic field in the disk as expected for a mean-field α - Ω dynamo. For an axisymmetric mode the magnetic field spirals in a uniform direction (Baryshnikova et al. 1987). Rotation curves show that the northeastern half is blueshifted whereas the southwestern half is redshifted (Pence 1981; Puche et al. 1991). Thus, the directions of the velocity and magnetic field are opposite to each

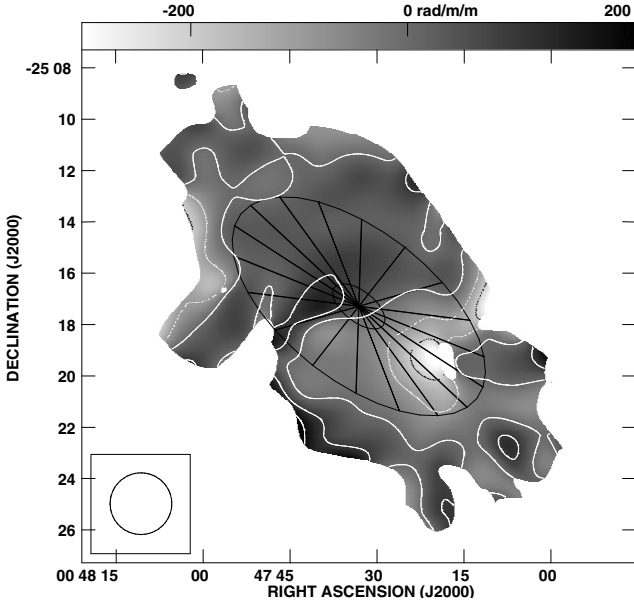


Fig. 8. RM distribution between $\lambda\lambda 6.2$ cm and 3.6 cm from Effelsberg observations at $144''$ resolution. Contours are at $-200, -100, 0, 100,$ and $200 \times 1 \text{ rad m}^{-2}$. The vector maps at both wavelengths were clipped below $4\times$ the rms noise level in polarized intensity prior to the combination. The sectors for the azimuthal RM variation are also shown (see Sect. 5.3).

other. Krause & Beck (1998) showed that for such a case the spiral magnetic field is pointing inwards.

Using the RM distribution we corrected the magnetic field orientation for the Faraday rotation. This was also done for the combined VLA + Effelsberg map at $\lambda 6.2$ cm shown in Fig. 5, although we do not have a RM map with sufficient resolution. We corrected the polarization angles for angular scales larger than $84''$ using a combined VLA + Effelsberg RM map (not shown). The Effelsberg polarization maps at $\lambda\lambda 6.2$ cm (Fig. 4) and 3.6 cm (Fig. 6) could be corrected without loss of resolution.

The effect of the Faraday correction is especially important at the the radio spur S1: the magnetic field vectors are almost perpendicular to the disk after applying the Faraday correction (a RM of 100 rad m^{-2} corresponds to a rotation of 15°). In general the Faraday correction made the magnetic field orientation more disk parallel in locations near the disk plane (compare Figs. 2 and 5).

5. The magnetic field structure

5.1. Axisymmetric model for the disk magnetic field

In Sect. 3 we suggested that the observed large-scale magnetic field is the superposition of a disk parallel and a vertical component. We will refer to the disk-parallel magnetic field with radial and azimuthal (r, ϕ) components as the *disk* magnetic field. The vertical magnetic field with radial and vertical (r, z) components we will refer to as the *halo* magnetic field.

As a model for the disk magnetic field we use a spiral magnetic field corresponding to an axisymmetric spiral (ASS) mode of a galactic dynamo, which is symmetric with respect to the plane (even parity). The inclination angle of the disk was prescribed as $i = 78.5^\circ$, which is that of the optical disk. For a pitch angle of $25^\circ \pm 5^\circ$ the polarized intensity of our model resembles the observed distribution (the optical pitch angle is 20°

(Pence 1981)). We fitted the observed polarized intensity along the major axis with a Gaussian distribution consisting of an inner disk ($FWHM = 6.5$ kpc) and an outer disk ($FWHM = 13$ kpc). For the vertical polarized emission profile we chose the exponential scaleheight of the synchrotron emission from the thin disk of 0.4 kpc at $\lambda 6.2$ cm (Paper I). We assumed energy equipartition between CRs and the magnetic field (where the CR number density is $n_{\text{CR}} \propto B^2$), so that the Gaussian $FWHM$ and the exponential scaleheight of the magnetic field are two and four times larger, respectively, than that of the synchrotron emission. The magnetic field has a $FWHM$ of 13 kpc and 26 kpc in the inner and outer disk, respectively, and a vertical scaleheight of 1.6 kpc. The profiles of the polarized flux density of the model and the observations are presented in Fig. 9. A summary of the model parameters can be found in Table 3.

We produced maps of Stokes Q and U by integrating along the line-of-sight

$$Q \propto n_{\text{CR}} B_{\perp}^2 \cdot \cos(2\psi) \quad U \propto n_{\text{CR}} B_{\perp}^2 \cdot \sin(2\psi), \quad (2)$$

where B_{\perp} is the component of the magnetic field perpendicular to the line-of-sight and ψ is the orientation angle of the local polarization vector. The maps were used to calculate the polarized emission and the orientation of the magnetic field. At this point we do not take any Faraday rotation into account but we will do so in Sect. 5.3. The ASS model for the disk magnetic field is shown in Fig. 10.

The model of the disk magnetic field clearly shows why the polarized emission is not symmetric with respect to the major and minor axis: the locations of the maxima of the polarized intensity are shifted due to the pitch angle in counterclockwise direction from the minor axis. Hence, the polarized intensity distribution resembles an S-shape, as observed. The depolarized regions D1 and D2 in the observed map of the polarized intensity (Fig. 5) can be explained by the model, too. They are located where different components of the magnetic field occur in one beam and thus cancel each other. We note that the magnetic field orientation is mainly disk parallel as expected for a spiral magnetic field. The good agreement between the model and the observed distribution in the disk justifies the choice of the model.

The comparison of the profiles of the polarized emission between the observations and the model in Fig. 9 shows that along the minor axis the halo shows up as additional emission. The halo magnetic field is investigated in the next section.

5.2. The halo magnetic field

The good agreement in the disk region of the simple model shown in Fig. 10 with the observations shows that the disk field dominates in the disk. We note that the two radio spurs are located near the two depolarized regions (D1 and D2 in Fig. 5), where the projected disk field has a minimum. Elsewhere the visibility of the halo field is reduced by the dominating disk field.

The observed polarized emission is the superposition of the disk and halo component with $Q = Q_{\text{d}} + Q_{\text{h}}$ and $U = U_{\text{d}} + U_{\text{h}}$. We subtracted the disk magnetic field model from the maps of Stokes Q and U of the combined VLA + Effelsberg observations at $\lambda 6.2$ cm. The polarized intensity and the orientation of the halo magnetic field was calculated from the maps of Q_{h} and U_{h} and is presented in Fig. 11.

The halo magnetic field clearly resembles an X-shape centered on the nucleus. Its orientation is mirror symmetric both to the major and minor axis. X-shaped halo fields have been observed in several edge-on galaxies with inclination angles

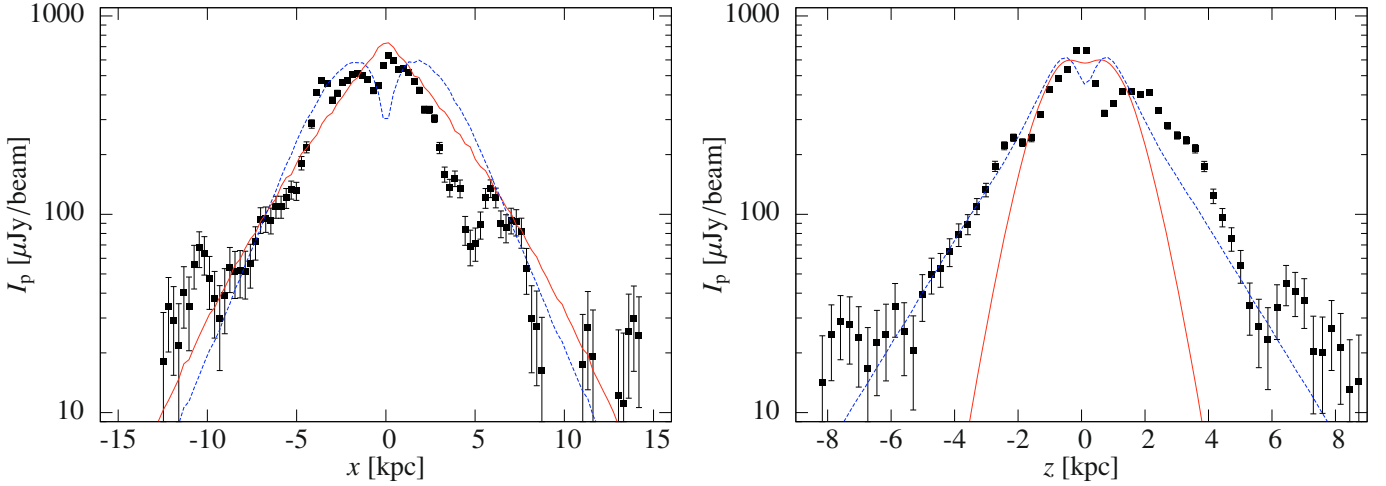


Fig. 9. Profiles of the polarized intensity along the major (*left*) and minor axis (*right*). The black symbols show the measured intensities from combined VLA + Effelsberg observations at $\lambda 6.2$ cm. The solid (red) lines show the distribution derived from the disk magnetic field model. The dashed (blue) lines show the model of the combined disk and halo magnetic field (see Sect. 5.3).

$i \geq 85^\circ$, almost edge-on (Krause et al. 2006; Krause 2007). This is the first galaxy with an X-shaped field which is only mildly edge-on ($i = 78.5^\circ$), so that the emission from the disk and halo are superimposed.

In order to quantify the halo magnetic field we determined the mean orientation angle $\widehat{\psi}$ in the four boxes shown in Fig. 11. We integrated Stokes Q and U and calculated the orientation angle of the magnetic field by

$$\widehat{\psi} = \left| \frac{1}{2} \arctan\left(\frac{U}{Q}\right) - p.a. + 90^\circ \right|, \quad (3)$$

where $p.a. = 52^\circ$ is the position angle of the major axis and $+90^\circ$ was included in order to convert the electric polarization angle into the magnetic field orientation. We find a mean orientation angle of $\widehat{\psi} = 46^\circ \pm 15^\circ$ with respect to the major axis.

5.3. Modeling the rotation measure distribution

An analysis of the RMs, averaged in sectors, as a function of the azimuthal angle θ gives further information about the structure of the large-scale magnetic field. The sector integration was applied between a galactocentric radius of 1.4 kpc and 6.7 kpc with a spacing of 20° in the azimuthal angle (see Fig. 8). An effective inclination of 60° describes the observed distribution of the polarized emission in the disk and halo at $\lambda 6.2$ cm with $144''$ resolution (Fig. 4). We chose the RM distribution at $144''$ resolution, because the low resolution favors the study of the large-scale RM structure.

The crosses in Fig. 12 give the azimuthal RM variation together with their errors. There is a broad maximum between 270° and 60° and the minimum is near $\theta = 180^\circ$. This confirms the result previously obtained from the morphology of the RM distribution: the northeastern half of the galaxy contains positive RMs ($-90^\circ \lesssim \theta \lesssim 90^\circ$) whereas the southwestern half of the galaxy contains negative RMs ($90^\circ \lesssim \theta \lesssim 270^\circ$).

The disk magnetic field is dominating the polarized emission. Therefore we will use the ASS model of the disk magnetic field in order to make a model for the RM distribution. We integrated the polarization vector along the line-of-sight, so that we take Faraday depth effects into account (Sokoloff et al. 1998). From the Emission Measure $EM = 10 \text{ cm}^{-6} \text{ pc}$

Table 3. Parameters used for the ASS model of the disk magnetic field.

| Parameter | Value | Notes |
|----------------------------|------------------------|-----------------------------|
| inclination angle i | 78.5° | optical disk |
| pitch angle | 25° | fitted to PI |
| magnetic field $FWHM$ | 13 kpc/26 kpc | fitted to PI profile |
| magnetic field scaleheight | 1.6 kpc | thin radio disk |
| ordered magnetic field | $3.0 \mu\text{G}$ | fitted to RM |
| electron $FWHM$ | 13 kpc | fitted to $H\alpha$ profile |
| electron scaleheight | 1.4 kpc | fitted to $H\alpha$ profile |
| electron density n_e | 0.05 cm^{-3} | from $H\alpha$ |

(Hoopes et al. 1996) we derived an electron density of $n_e = 0.05 \text{ cm}^{-3}$, where we assumed a pathlength of 6.5 kpc. From the $H\alpha$ distribution we derived a Gaussian distribution of the electron density along the major axis with a $FWHM$ of 13 kpc and a vertical scaleheight of 1.4 kpc. The RM distribution of the ASS model is presented in Fig. 13. It is notably asymmetric where the minimum has a larger amplitude than the maximum.

Averaging Stokes Q and U of our ASS magnetic field model in sectors provides the azimuthal RM variation shown as solid line in Fig. 12. We found reasonable agreement with the observed variation for an ordered magnetic field strength of $3.0 \pm 0.5 \mu\text{G}$. From pulsar RMs we obtain a foreground of $RM_{\text{for}} = 10 \pm 5 \text{ rad m}^{-2}$ at the position of NGC 253, which is near to the Galactic south pole (Noutsos et al. 2008). Compared with the amplitude of the RM variation the foreground RM is $\approx 10\%$, which we further neglect in our analysis.

The azimuthal RM variation of a spiral ASS field in an RM screen or a homogeneous, mildly inclined emitting layer can be described by a simple cosine, with a phase shift $\Delta\theta$ equal to the pitch angle of the magnetic field spiral (Krause et al. 1989). However, the strongly inclined disk of NGC 253 requires to take into account the distribution of Faraday depths along the line-of-sight.

Our model can explain the observations much better than the cosine variation of an RM screen. For the screen the amplitudes of the maximum and the minimum are equal, whereas our model can reproduce both the maximum with $RM \approx 120 \text{ rad m}^{-2}$ and the minimum $RM \approx -180 \text{ rad m}^{-2}$. Furthermore, the RM screen predicts the maximum at $\Delta\theta$ but our model shows that the

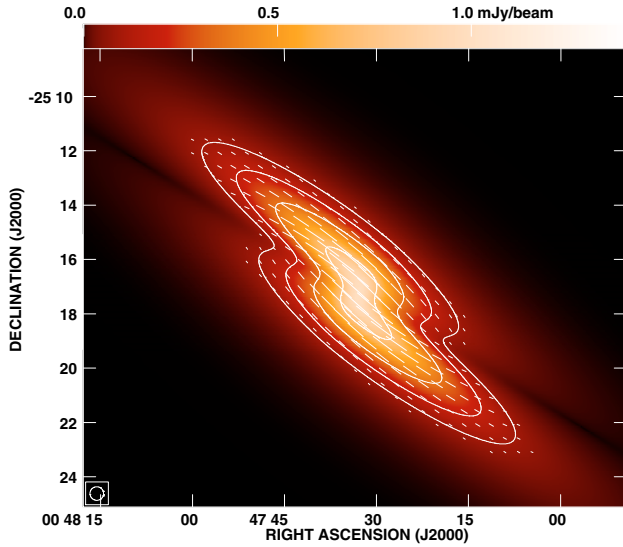


Fig. 10. Modeled polarized intensity at $\lambda 6.2$ cm of the axisymmetric magnetic field (ASS) of the disk at $30''$ resolution. Contours are at $3, 6, 12,$ and $24 \times 30 \mu\text{Jy}/\text{beam}$ of polarized intensity. The vectors indicate the magnetic field orientation where the length of the vectors of $1''$ is equivalent to $12.5 \mu\text{Jy}/\text{beam}$ polarized intensity.

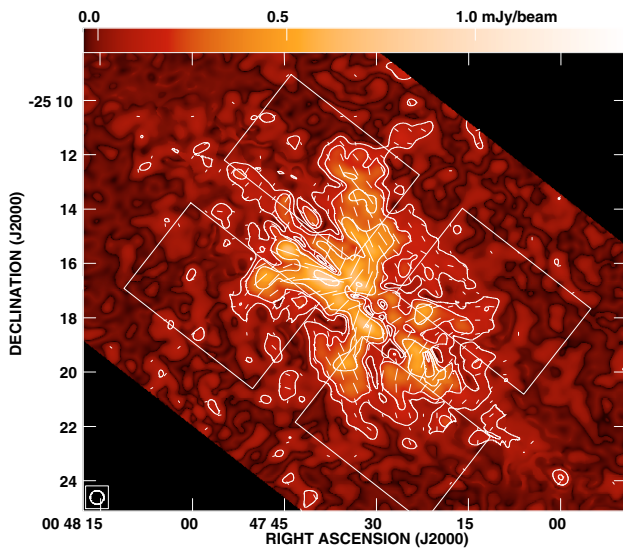


Fig. 11. Polarized intensity at $\lambda 6.2$ cm of the halo magnetic field with $30''$ resolution after subtraction of the disk field model. Contours and vectors are identical to Fig. 10. The boxes for the integration of the orientation angle $\hat{\psi}$ are also shown.

maximum is very broad, in agreement with the observations. This can be explained by the thickness of the disk (not a thin emitting layer) and the inclination of the disk together with the smearing by the observation beam. The difference in amplitude between the maximum and minimum is a strong function of inclination.

The model of the disk magnetic field alone fits already to the observed RM variation (reduced $\chi^2 = 6.5$). But so far we took not into account the halo magnetic field that we also observe and which contributes significantly to the polarized emission. With observations at only two wavelengths there is no direct way to decompose the observed RM of the disk and halo magnetic field, because they are overlapping along the line-of-sight. Still, we can produce a model including the halo and disk magnetic fields.

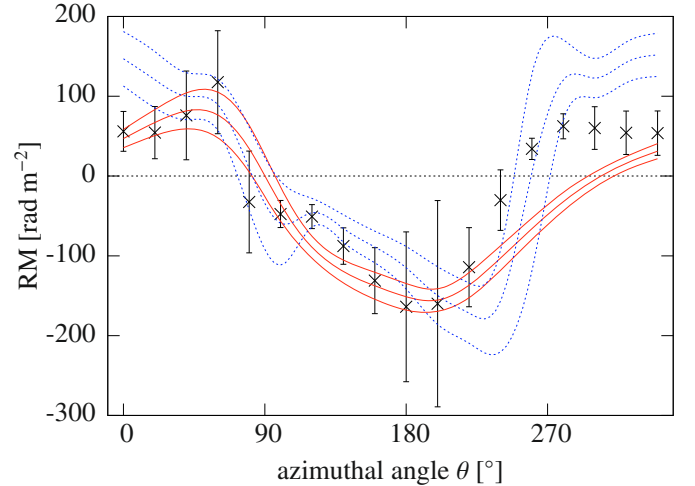


Fig. 12. RM variation as a function of the azimuthal angle θ . The crosses give the observed RMs averaged in sectors as shown in Fig. 8 and their errors. The solid (red) lines represents the ASS model of the disk magnetic field together with its error interval. The dashed (blue) lines shows the model of the combined disk and halo magnetic field (and its error interval) which are both of even parity.

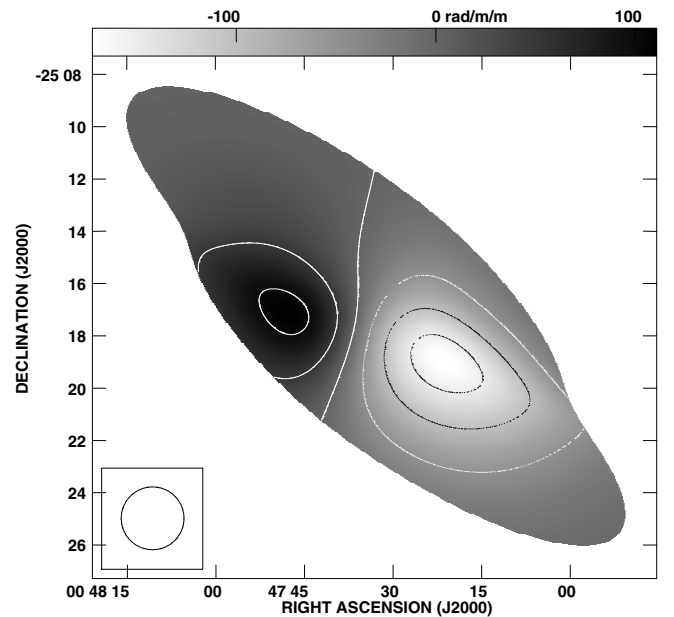


Fig. 13. RM distribution of the axisymmetric spiral (ASS) of the disk magnetic field at $144''$ resolution. Contours are at $-150, -100, -50, 0, 50,$ and $100 \times 1 \text{ rad m}^{-2}$. The map was clipped at $0.2 \text{ mJy}/\text{beam}$ in polarized intensity.

For the halo magnetic field we propose a model where the field lines are along a cone above and below the galactic plane, so that in projection to the plane of the sky the field forms an X-shape. From the orientation angle of the halo magnetic field as derived in Sect. 5.2 we deduce an opening angle of the cone of $180^\circ - 2 \times \hat{\psi} = 90^\circ \pm 30^\circ$. Note that the contributions to the RM do not cancel if the line-of-sight components of the field change sign along the line-of-sight, as is the case in our cone model, because of different pathlengths towards the cone's far and near sides. Hence, we see the RM mainly from the front half of the cone.

For the same reason we can only see the field direction in the southern halo, because it lies in front of the bright disk and

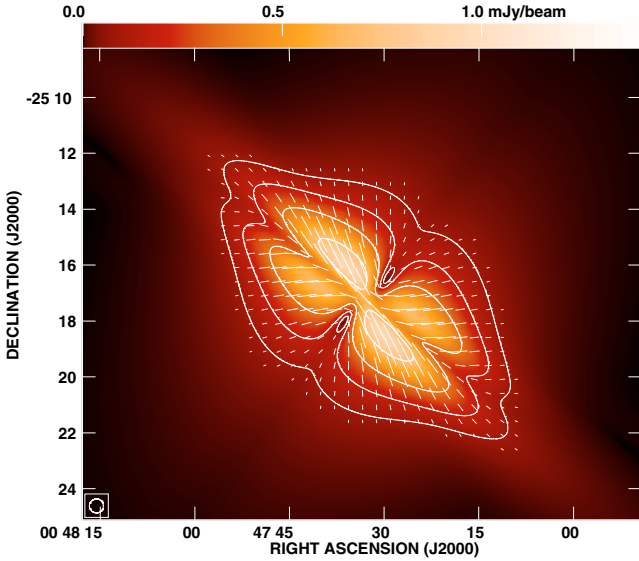


Fig. 14. Modeled polarized intensity at $\lambda 6.2$ cm of the combined even disk and even halo magnetic field at $30''$ resolution. Contours are at 3, 6, 12, and $24 \times 30 \mu\text{Jy}/\text{beam}$ of polarized intensity. The vectors indicate the magnetic field orientation (corrected for Faraday rotation) where the length of the vectors of $1''$ is equivalent to $12.5 \mu\text{Jy}/\text{beam}$ polarized intensity. This figure corresponds to the model shown in Fig. A.5.

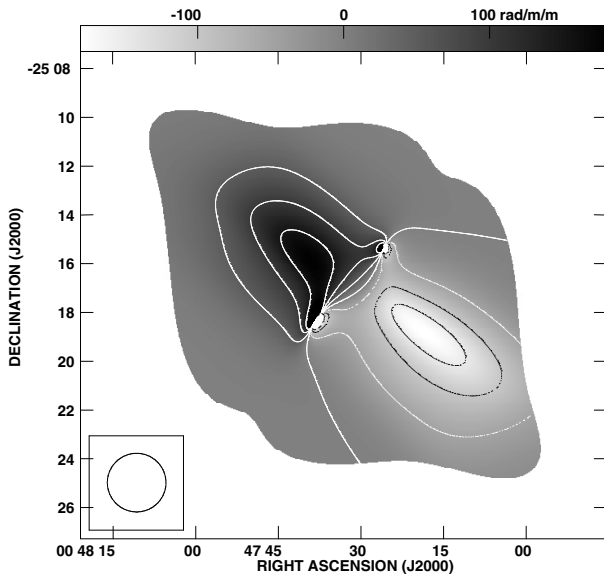


Fig. 15. Model RM distribution for the combined even disk and even halo magnetic field at $144''$ resolution. Contours are at -150 , -100 , -50 , 0 , 50 , 100 and $150 \times 1 \text{ rad m}^{-2}$. This figure is identical with the Fig. A.5c.

acts therefore as a Faraday screen. Our models show that the magnetic field points away from the disk in the southern halo. In case that the field points also away from the disk in the northern halo, the halo field has *even* parity. Otherwise, if the field points towards the disk in the northern halo, the halo field has *odd* parity. Because the field direction in the northern halo has only a small influence on the RM distribution the difference of the azimuthal RM variation is also small. We tested all possible combinations of disk and halo magnetic field configurations. The result is summarized in a catalog in Appendix A. The disk magnetic field is of even parity, where the field is pointing in the same direction above and below the galactic midplane. An odd disk

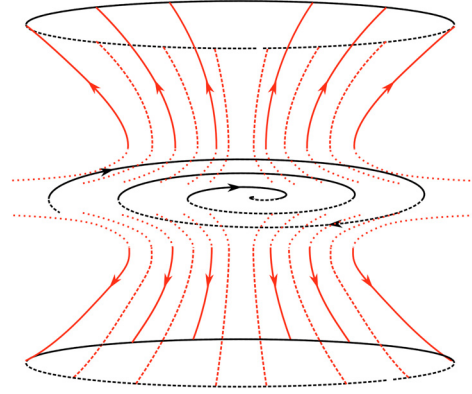


Fig. 16. Sketch of the observable components of the large-scale magnetic field structure. In the disk, the ASS spiral magnetic field is even and pointing inwards. In the halo, the magnetic field is also even and pointing outwards. Dashed lines indicate components on the rear side. The dotted part of the halo magnetic field is not observed.

magnetic field in combination with any halo magnetic field leads to strong local gradients in the RM distribution which are not observed. The even disk field together with an even halo field fits slightly better to the observations with a reduced $\chi^2 = 4.9$ (see Fig. 12) than with an odd halo field with $\chi^2 = 13$ (see Fig. A.7). The polarized intensity and the RM distribution of our favored model for the combined even disk and even halo magnetic field is shown in Figs. 14 and 15. A sketch of the magnetic field lines is presented in Fig. 16⁷.

We investigated also the possibility of an azimuthal halo magnetic field component which is predicted by some halo models (Dalla Vecchia & Schaye 2008; Wang & Abel 2009). It was included into the conical magnetic field model and the RM variation of the combined disk and halo model was studied. It turned out that the azimuthal component – if there is any – must point in the opposite direction to that of the disk magnetic field. As an upper limit of the azimuthal component we estimate 60% of the field strength ($\chi^2 = 3.9$). We note that the shape and direction of the model halo magnetic field is still consistent with the observations, i.e. is not very sensitive to the relative strength of the azimuthal component.

5.4. Magnetic field strengths

The magnetic field strength can be calculated using the energy equipartition assumption as described in Beck & Krause (2005). As in Paper I we use a pathlength through the total power emission of 6.5 kpc and a CR proton to electron ratio of $K = 100$, and a nonthermal radio spectral index of 1.0. With a typical nonthermal total power flux density of $8 \text{ mJy}/\text{beam}$ at $\lambda 6.2$ cm with $30''$ resolution we find a total magnetic field strength of $15 \pm 1.5 \mu\text{G}$ in the disk. At a polarization degree of 5% this corresponds to $4.4 \pm 0.5 \mu\text{G}$ for the ordered magnetic field in the disk. The strength of the halo magnetic field was estimated by fitting profiles of the polarized emission to the observations (see Fig. 9). We found $4.4 \pm 0.5 \mu\text{G}$ for the halo magnetic field.

We now compare the magnetic field strengths of the ordered field calculated from the equipartition and from the RM analysis.

⁷ The magnetic field lines are schematically shown for the observed components only. We miss structures that are smaller than our resolution element and regions where not enough CR electrons are present. Therefore, all field lines are closed by components that we do not observe.

The equipartition value can be larger than that of the RM analysis, because the anisotropic turbulent magnetic field emits polarized emission but does not or only weakly contribute to the observed RM (Beck et al. 2005). From the azimuthal RM variation of our modeled ASS disk field we found an ordered magnetic field component of $3.0 \pm 0.5 \mu\text{G}$ for the disk. In the halo, the magnetic field strength is similar with $3.0 \pm 0.5 \mu\text{G}$. There may be some anisotropic field component both in the disk and halo because the equipartition strength of the ordered magnetic field is about 50% larger than that of the RM analysis. The anisotropic field component can contribute significantly to the polarized emission in galaxies as shown for NGC 1097 (Beck et al. 2005) and M 51 (Fletcher et al. 2010).

6. Discussion

6.1. The superwind model

NGC 253 is a prototypical nuclear starburst galaxy, which is the source of an outflow of hot X-ray emitting gas (Strickland et al. 2000; Bauer et al. 2007). Spectroscopic measurements of H α -emitting gas in the southern nuclear outflow cone by Schulz & Wegner (1992) give an outflow velocity of 390 km s^{-1} . Apart from the nuclear outflow, huge lobes of diffuse X-ray emission in the halo are extending up to 8 kpc away from the disk. These lobes are thought to be the walls of two huge bubbles containing a hot gas with a low density (Pietsch et al. 2000; Strickland et al. 2002). Sensitive XMM-Newton observations revealed that indeed the entire bubbles are filled with X-ray emitting gas (Bauer et al. 2008). Similar structures are found in other galaxies with intense star formation, with M 82 as the most prominent example, and are now known as *superwinds* (Heckman et al. 2000).

Figure 17 shows the diffuse H α emission in greyscale. There are several H α plumes extending from the disk into the halo. We note that the large plume east of the nucleus corresponds to the radio spur S1 (see Fig. 5). The diffuse X-ray emission in Fig. 18 shows a similar structure with the lobe at the extension E1 extending furthest into the halo. The abundance of heated gas has an asymmetry with respect to the minor axis: the northeastern half contains significantly more diffuse H α and soft X-ray emission than the southwestern half which cannot be explained by a symmetric superwind. This asymmetry is also observed in HI emission (Boomsma et al. 2005) which surrounds the superbubbles. An explanation is attempted in Sect. 6.4.

6.2. The disk wind model

The halo magnetic field allows CRs to stream along the field lines from the disk into the halo. In Paper I we determined the vertical CR bulk speed as $v_{\text{CR}} = 300 \pm 30 \text{ km s}^{-1}$ which is remarkably constant over the entire extent of the disk. This shows the existence of a disk wind in NGC 253. CRs cannot stream faster than with Alfvén speed with respect to the magnetic field, because they are scattered at self-excited Alfvén waves via the so-called streaming instability (Kulsrud & Pearce 1969). A typical magnetic field strength of $B \approx 15 \mu\text{G}$ and a density of the warm gas of $n \approx 0.05 \text{ cm}^{-3}$ (Sect. 3.5) leads to an Alfvén speed of $v_A = B/\sqrt{4\pi\rho} \approx 150 \text{ km s}^{-1}$. The super-Alfvénic CR bulk speed requires that the CRs and the magnetic field are advectively transported together in the disk wind. CRs stream with Alfvén speed with respect to the magnetic field that is frozen into the thermal gas of the wind. The measured CR bulk speed is the superposition $v_{\text{CR}} = v_W + v_A$ of the outflow speed of the thermal gas v_W in the wind and the Alfvén speed v_A

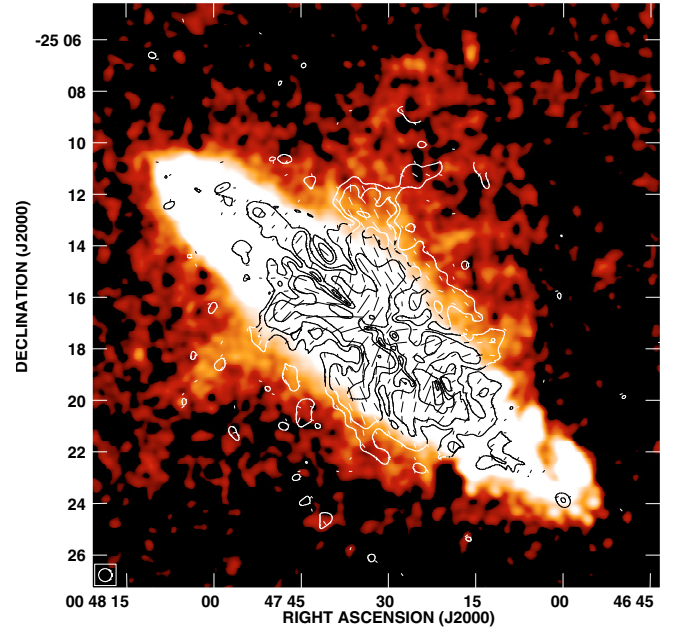


Fig. 17. Halo magnetic field overlaid onto diffuse H α emission as greyscale. Contours are at $3, 6, 12,$ and $24 \times 30 \mu\text{Jy}/\text{beam}$ (the rms noise level). A vector length of $1''$ is equivalent to $12.5 \mu\text{Jy}/\text{beam}$ polarized intensity. The H α map from Hoopes et al. (1996) was convolved with a Gaussian to $20''$ resolution in order to show the weak diffuse emission in the halo.

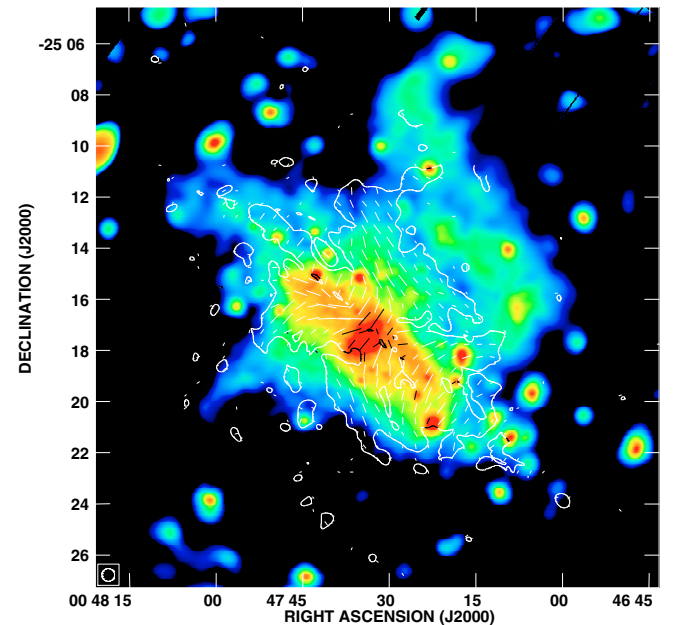


Fig. 18. Halo magnetic field overlaid onto diffuse X-ray emission. The contour is at $3 \times 30 \mu\text{Jy}/\text{beam}$ (the rms noise level). A vector length of $1''$ is equivalent to $12.5 \mu\text{Jy}/\text{beam}$ polarized intensity. The X-ray map is from XMM-Newton observations in the energy band $0.5\text{--}1.0 \text{ keV}$ (Bauer et al. 2008).

(Breitschwerdt et al. 2002). Adopting this picture the wind speed at the galactic midplane in NGC 253 is $v_W \approx 150 \text{ km s}^{-1}$. The Alfvén speed is difficult to estimate, so that the uncertainty in the actual value of the wind speed is large as well. Furthermore, we could measure only the average wind speed between 1 kpc and 5 kpc above the plane. Therefore, the bulk speed near the galactic midplane may be lower than 150 km s^{-1} . Studies of CR

transport in a galactic wind by [Breitschwerdt et al. \(1991\)](#) and follow-up works assumed a wind speed of only a few 10 km s^{-1} at the starting point in the galactic midplane which accelerates to the escape velocity at larger distances to the disk ([Breitschwerdt et al. 1993](#); [Zirakashvili et al. 1996](#); [Breitschwerdt et al. 2002](#)). On the other hand, [Everett et al. \(2008\)](#) found a high wind speed of 170 km s^{-1} in the plane of the Milky Way in order to explain the soft X-ray emission in the halo. Our value measured in NGC 253 does not exclude any of these models. It will be left to future observations to provide an accurate estimate of the wind speed at different heights above the galactic plane.

If the large-scale magnetic field is frozen into the thermal gas in the wind the halo magnetic field has an azimuthal component and winds up in a spiral. The field configuration is similar to that of the sun with the Parker spiral magnetic field ([Parker 1958](#); [Weber & Davis 1967](#)). The azimuthal component increases with height, so that above a certain height the magnetic field is almost purely azimuthal. Up to the Alfvénic point the stiff magnetic field lines corotate with the underlying disk. If the azimuthal component of the halo magnetic field is small, the observable radio halo is within the corotating regime and the Alfvén radius is larger than the vertical extent of the halo. As an azimuthal halo component cannot be excluded (Sect. 5.3), the Alfvénic radius may be smaller than 2 kpc, which is the scaleheight of the polarized emission in the halo.

The existence of a disk wind has important consequences for the transport of angular momentum. As we have shown in Paper I the CR bulk speed is fairly constant over the extent of the disk, i.e. it does not depend on the galactocentric radius. If this is also true for the speed of the disk wind, angular momentum is effectively transported to large galactocentric radii ([Zirakashvili et al. 1996](#)). Moreover, the angular momentum of the wind per unit wind mass is proportional to the Alfvén radius as shown by [Zirakashvili et al. \(1996\)](#). An Alfvén radius of ≈ 2 kpc agrees with their models for which they found a significant loss of angular momentum over the lifetime of a galaxy. We note that the disk wind can account for larger angular momentum losses than the superwind in the center (at small galactocentric radii).

6.3. The origin of X-shaped halo magnetic fields

The distribution of the halo magnetic field is X-shaped in both orientation and intensity. As the intensity of the polarized emission depends on the perpendicular component of the ordered field, a possible explanation of the intensity distribution is limb brightening in the conical halo magnetic field. We modeled this effect using a halo magnetic field lying on a cone with an opening angle of 90° and the inclination angle of NGC 253. The model can reproduce indeed an increased vertical extension along the limbs.

The halo magnetic field follows the lobes of the heated gas that are regarded as walls of huge bubbles expanding into the surrounding medium. The large-scale magnetic field may be compressed and aligned by shock waves in the walls. These shock waves are also able to heat a pre-existing cold halo gas, so that the gas becomes visible as $\text{H}\alpha$ and soft X-ray emission. The cold halo gas seen in HI emission surrounds the superbubbles and shows the same asymmetric distribution as expected if this gas is the source for the heated gas in the halo. A cartoon of the halo structure including the large-scale magnetic field is shown in Fig. 19.

Both the disk wind model and the superwind model, in conjunction with a large-scale dynamo action, can explain the X-shaped halo magnetic field. We should note, however, that

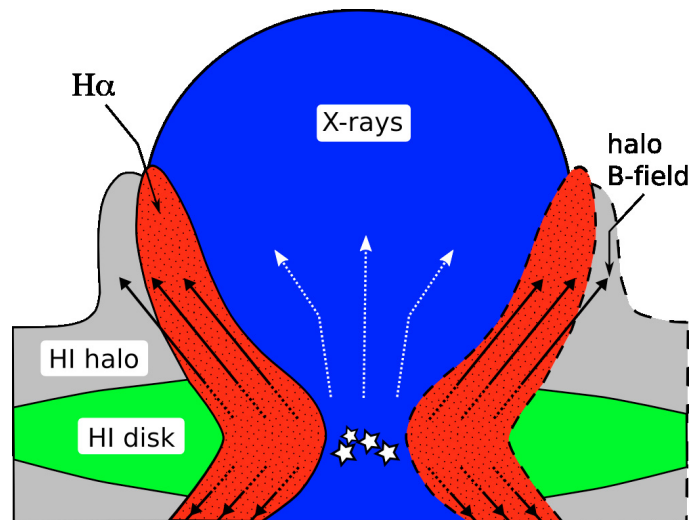


Fig. 19. Halo structure of NGC 253. Reproduced from [Boomsma et al. \(2005\)](#) and extended. The superbubble, filled with soft X-rays emitting gas, expands into the surrounding medium (indicated by dotted lines with arrows). The halo magnetic field is aligned with the walls of the superbubble. Dashed lines denote components that are not (or only weakly) detected in the southwestern half of NGC 253.

such magnetic field structures are observed in several edge-on galaxies. These galaxies show a very different level of star formation ([Krause 2009](#)). Most of them do not possess a starburst in the center and hence they have no superwind. While the classical α - Ω dynamo can not explain such an X-shaped halo field, model calculations of a galactic disk within a spherical halo including a galactic wind showed a similar magnetic field configuration ([Brandenburg et al. 1993](#)). Hydrodynamical simulations show that the wind in spiral galaxies has a significant radial component due to the radial gradient of the gravitational potential. The wind flow reveals an X-shape when the galaxy is seen edge-on ([Dalla Vecchia & Schaye 2008](#)). New MHD simulations of disk galaxies including a galactic wind are in progress and may explain the halo X-shaped field ([Gressel et al. 2008](#); [Hanasz et al. 2009a,b](#)). The first global galactic-scale MHD simulations of a CR-driven dynamo give very promising results showing directly that magnetic flux is transported from the disk into the halo ([Hanasz et al. 2009c](#)). Therefore we suggest that in NGC 253 the X-shaped halo field is connected rather to the disk wind than to the superwind. The superwind gas flow may be collimated by the halo magnetic field.

The transport of CRs and magnetic fields has important consequences for the possibility of a working dynamo in NGC 253. The α - Ω dynamo relies on the differential rotation of the galactic disk (Ω -effect) and the cyclonic motions of the ionized gas (α -effect). The latter one can be generated by subsequent supernova explosions ([Ferrière 1992](#)). The amplification of magnetic fields by an α - Ω dynamo requires expulsion of small-scale helical fields (see e.g. [Brandenburg & Subramanian 2005](#)). [Sur et al. \(2007\)](#) showed that galactic winds can transport the helicity flux by advection. A galactic wind may be thus vital for a working dynamo.

6.4. The origin of the gas in the halo

The cold gas in the halo of NGC 253 is necessary to explain the halo structure with the superwind model. Its origin, however, is yet unknown. [Boomsma et al. \(2005\)](#) discussed a gas infall in

NGC 253 by a minor merger to explain the asymmetric H I halo distribution with respect to the minor axis. But they noted that a minor merger event is unlikely because the distribution of H I is very symmetric with respect to the major axis. Could the disk wind be the origin of the cold gas in the halo? The disk wind is asymmetric with respect to the minor axis. The convective north-eastern half indicates a strong disk wind which transports gas from the disk into the halo while in the diffusive southwestern half the wind is weaker (Paper I).

We can only speculate about the reason why the two halo parts are so different. Star formation in the disk most likely plays an important role. The northeastern spiral arm contains significantly more H II regions than the southwestern one as is visible from Fig. 4b in Hoopes et al. (1996). Moreover, the amount of total radio continuum emission indicates a higher star-formation rate in this part of the disk. Since the energy input of star formation is essential for the injection of thermal and CR gas, the disk wind can be more easily driven in the northeastern half. Thus, the disk wind is a good candidate for the origin of the cold gas in the halo.

7. Summary and conclusions

The three-dimensional magnetic field structure can be investigated using sensitive radio continuum polarimetry. Our main results are:

1. A disk parallel magnetic field exists along the midplane of the disk. The magnetic field lines are slowly opening further away from the midplane. The vertical magnetic field component is most prominent at the edge of the inner disk where we find two “radio spurs”, one previously known east of the nucleus and one newly discovered west of the nucleus. The magnetic field configuration can be described as an X-shaped pattern, as in other edge-on galaxies.
2. The large-scale magnetic field can be decomposed into a disk (r, ϕ) and a halo (r, z) component.
3. The disk magnetic field of NGC 253 can be described by an axisymmetric spiral (ASS) magnetic field with a constant pitch angle of $25^\circ \pm 5^\circ$ which is symmetric with respect to the plane. This model shows a high resemblance to the observed magnetic field in the disk.
4. The distribution of the polarized intensity and the orientation of the halo magnetic field shows a distinct X-shaped pattern centered on the nucleus. Our model of the disk magnetic field was subtracted to construct a map of the halo magnetic field. We propose a model where the halo field lines are along a cone with an opening angle of $90^\circ \pm 30^\circ$ and are pointing away from the disk (even parity). An odd halo magnetic field is also possible, because we can not reliably determine the magnetic field direction in the northern halo.
5. The distribution of the halo magnetic field coincides in shape with the extra-planar heated gas traced by H α and soft X-ray emission. Possible explanations are limb brightening and compression of the halo magnetic field in the walls of the expanding superbubbles.
6. A disk wind plus dynamo action is a promising scenario for the origin of the gas in the halo and for the expulsion of small-scale helical fields as requested for efficient dynamo action. The disk wind can also account for large angular momentum and magnetic flux losses over galactic time scales.

Future investigations should include polarimetry at low frequencies, to take advantage of studying the magnetic structure far

away from the disk illuminated by an aged population of CR electrons. This should become feasible with the upcoming class of telescopes operating at low frequencies like LOFAR and the low-frequency SKA array. RM Synthesis (Brentjens & de Bruyn 2005; Heald et al. 2009) applied to multi-channel polarization observations is required to separate the RM contributions from the disk and the halo of strongly inclined galaxies.

Acknowledgements. VH acknowledges the funding by the Graduiertenkolleg GRK 787 and the Sonderforschungsbereich SFB 591 during the course of his PhD. The GRK 787 “Galaxy groups as laboratories for baryonic and dark matter” and the SFB 591 “Universal properties of non-equilibrium plasmas” are funded by the Deutsche Forschungsgemeinschaft (DFG). RJJ is supported by DFG in the framework of the research unit FOR 1048.

We thank Dieter Breitschwerdt and Andrew Fletcher for many fruitful discussions. Moreover, we would like to thank Charles Hoopes for kindly providing us his H α map of NGC 253. We thank Michael Bauer for providing us the XMM-Newton map. We are grateful to Elly Berkhuijsen and Matthias Ehle for carefully reading the manuscript and suggesting many improvements to the paper.

References

- Baryshnikova, I., Shukurov, A., Ruzmaikin, A., et al. 1987, *A&A*, 177, 27
 Bauer, M., Pietsch, W., Trinchieri, G., et al. 2007, *A&A*, 467, 979
 Bauer, M., Pietsch, W., Trinchieri, G., et al. 2008, *A&A*, 489, 1029
 Beck, R. 2007, *A&A*, 470, 539
 Beck, R., & Krause, M. 2005, *AN*, 326, 414
 Beck, R., Carilli, C. L., Holdaway, M. A., et al. 1994, *A&A*, 292, 409
 Beck, R., Brandenburg, A., Moss, D., Shukurov, A., & Sokoloff, D. 1996, *ARA&A*, 34, 155
 Beck, R., Fletcher, A., Shukurov, A., et al. 2005, *A&A*, 444, 739
 Boomsma, R., Oosterloo, T., Fraternali, F., van der Hulst, J. M., & Sancisi, R. 2005, *A&A*, 431, 65
 Brandenburg, A., & Subramanian, K. 2005, *Phys. Rep.*, 417, 1
 Brandenburg, A., Donner, K. J., Moss, D., et al. 1993, *A&A*, 271, 36
 Braun, R. 1988, *Millimeter Array Memo*, 46
 Breitschwerdt, D. 2003, in *Rev. Mex. Astron. Astrofis. Conf. Ser.* 15, ed. J. Arthur, & W. J. Henney, 311
 Breitschwerdt, D., McKenzie, J. F., & Völk, H. J. 1991, *A&A*, 245, 79
 Breitschwerdt, D., McKenzie, J. F., & Völk, H. J. 1993, *A&A*, 269, 54
 Breitschwerdt, D., Dogiel, V. A., & Völk, H. J. 2002, *A&A*, 385, 216
 Brentjens, M. A., & de Bruyn, A. G. 2005, *A&A*, 441, 1217
 Carilli, C. L., Holdaway, M. A., Ho, P. T. P., et al. 1992, *ApJ*, 399, L59
 Chyży, K. T. 2008, *A&A*, 482, 755
 Chyży, K. T., & Beck, R. 2004, *A&A*, 417, 541
 Chyży, K. T., Ehle, M., & Beck, R. 2007, *A&A*, 474, 415
 Dahlem, M., Lisenfeld, U., & Golla, G. 1995, *ApJ*, 444, 119
 Dahlem, M., Lisenfeld, U., & Rossa, J. 2006, *A&A*, 457, 121
 Dalla Vecchia, C., & Schaye, J. 2008, *MNRAS*, 387, 1431
 Dettmar, R.-J. 1992, *Fundamentals of Cosmic Physics*, 15, 143
 Dettmar, R.-J., & Soida, M. 2006, *AN*, 327, 495
 Dumke, M., & Krause, M. 1998, in *The Local Bubble and Beyond*, ed. D. Breitschwerdt, M. J. Freyberg, & J. Trümper, *Lect. Notes Phys.* 506 (Berlin: Springer Verlag), IAU Colloq., 166, 555
 Everett, J. E., Zweibel, E. G., Benjamin, R. A., et al. 2008, *ApJ*, 674, 258
 Ferrière, K. 1992, *ApJ*, 391, 188
 Fletcher, A., Beck, R., Shukurov, A., Berkhuijsen, E. M. & Horellou, C. 2010, in prep.
 Golla, G., & Hummel, E. 1994, *A&A*, 284, 777
 Gressel, O., Elstner, D., Ziegler, U., et al. 2008, *A&A*, 486, L35
 Hanasz, M., Otmianowska-Mazur, K., Kowal, G., et al. 2009a, *A&A*, 498, 335
 Hanasz, M., Otmianowska-Mazur, K., Lesch, H., et al. 2009b, in *IAU Symp.*, 259, 479
 Hanasz, M., Wólczyński, D., Kowalik, K., et al. 2009c, in *IAU Symp.*, 259, 549
 Heald, G., Braun, R., & Edmonds, R. 2009, *A&A*, 503, 409
 Heckman, T. M., Lehnert, M. D., Strickland, D. K., et al. 2000, *ApJS*, 129, 493
 Heesen, V. 2008, Ph.D. Thesis, Ruhr-Universität Bochum, Germany
 Heesen, V., Beck, R., Krause, M., et al. 2009, *A&A*, 494, 563
 Hoopes, C. G., Walterbos, R. A. M., & Greenwalt, B. E. 1996, *AJ*, 112, 1429
 Ipavich, F. M. 1975, *ApJ*, 196, 107
 Karachentsev, I. D., Grebel, E. K., Sharina, M. E., et al. 2003, *A&A*, 404, 93
 Krause, F., & Beck, R. 1998, *A&A*, 335, 789
 Krause, M. 2004, in *The Magnetized Interstellar Medium*, ed. B. Uyaniker, W. Reich, & R. Wielebinski, 173

- Krause, M. 2007, in *Mem. della Soc. Astron. Ital.*, 78, 314
- Krause, M. 2009, in , *Magnetic Fields in the Universe II*, ed. A. Esquivel, *RevMexAA*, 36, 25
- Krause, M., Hummel, E., & Beck, R. 1989, *A&A*, 217, 4
- Krause, M., Wielebinski, R., & Dumke, M. 2006, *A&A*, 448, 133
- Kulsrud, R., & Pearce, W. P. 1969, *ApJ*, 156, 445
- Mac Low, M.-M., & Ferrara, A. 1999, *ApJ*, 513, 142
- Norman, C. A., & Ikeuchi, S. 1989, *ApJ*, 345, 372
- Noutsos, A., Johnston, S., Kramer, M., et al. 2008, *MNRAS*, 386, 1881
- Parker, E. N. 1958, *ApJ*, 128, 664
- Parker, E. N. 1992, *ApJ*, 401, 137
- Pence, W. D. 1981, *ApJ*, 247, 473
- Pietsch, W., Vogler, A., Klein, U., et al. 2000, *A&A*, 360, 24
- Pietsch, W., Roberts, T. P., Sako, M., et al. 2001, *A&A*, 365, L174
- Puche, D., Carignan, C., & van Gorkom, J. H. 1991, *AJ*, 101, 456
- Schlickeiser, R. 2002, *Cosmic Ray Astrophysics* (Berlin, Germany: Springer)
- Schulz, H., & Wegner, G. 1992, *A&A*, 266, 167
- Soida, M., Otmianowska-Mazur, K., Chyży, K., et al. 2006, *A&A*, 458, 727
- Sokoloff, D. D., Bykov, A. A., Shukurov, A., et al. 1998, *MNRAS*, 299, 189
- Strickland, D. K., Heckman, T. M., Weaver, K. A., et al. 2000, *AJ*, 120, 2965
- Strickland, D. K., Heckman, T. M., Weaver, K. A., Hoopes, C. G., & Dahlem, M. 2002, *ApJ*, 568, 689
- Sur, S., Shukurov, A., & Subramanian, K. 2007, *MNRAS*, 377, 874
- Tüllmann, R., Dettmar, R.-J., Soida, M., Urbanik, M., & Rossa, J. 2000, *A&A*, 364, L36
- Vollmer, B., Soida, M., Chung, A., et al. 2008, *A&A*, 483, 89
- Wang, P., & Abel, T. 2009, *ApJ*, 696, 96
- Weber, E. J., & Davis, L. J. 1967, *ApJ*, 148, 217
- Weżgowiec, M., Urbanik, M., Vollmer, B., et al. 2007, *A&A*, 471, 93
- Zirakashvili, V. N., Breitschwerdt, D., Ptuskin, V. S., et al. 1996, *A&A*, 311, 113

Appendix A: Magnetic field models

In order to find the best model for the magnetic field in NGC 253 we studied the expected polarized intensities and RMs of various possibilities of the disk and halo magnetic field alone and combinations of them. The setup of the models is described in Sect. 5.1 with the parameters of Table 3. In Figs. A.1–A.12 we present the polarized intensity and the magnetic field orientation (not corrected for Faraday rotation) for $\lambda\lambda$ 6.2 cm (a) and 3.6 cm (b) at 30'' resolution. Note that the Faraday corrected magnetic field orientation is identical for all models consisting both of the disk and halo field (Figs. A.5–A.12). The difference in the models is only in the *direction* of the magnetic field that becomes visible in the RM distribution (c) shown with 144'' resolution. Sketches (d) show the direction of the magnetic field in the disk and in the halo. Here, a “.” indicates that the field points to the observer and a “+” denotes a field pointing away.

Figures A.1 and A.2 show the disk magnetic field alone for the even and odd case. They are similar but the odd field has a smaller amplitude in the RM distribution. This can be understood as the scaleheight of the disk is smaller than the projected minor axis. We see therefore only one side of the disk (the southern one). Figures A.3 and A.4 show the halo magnetic field alone for the even and odd cases. Note the asymmetry of both the polarized intensity and the RM. Because the magnetic field orientation changes along the line-of-sight, there is some depolarization as the magnetic field vectors are not parallel to each other. If the Faraday rotation has the same sense as the rotation of the magnetic field, the depolarization is stronger. If they have opposite senses, the depolarization is weaker. This can explain the asymmetry although the magnetic field is axisymmetric.

Figures A.5–A.8 show the models with the even disk magnetic field. Among them Figs. A.5 and A.7 are the models whose RM distribution agrees best with the observations. The two models only differ in the direction of the northern halo field. The even halo magnetic field (Fig. A.5) is our best-fit model. Figures A.9–A.12 show the models for an odd disk magnetic field. They all have strong gradients in the RM which are not observed.

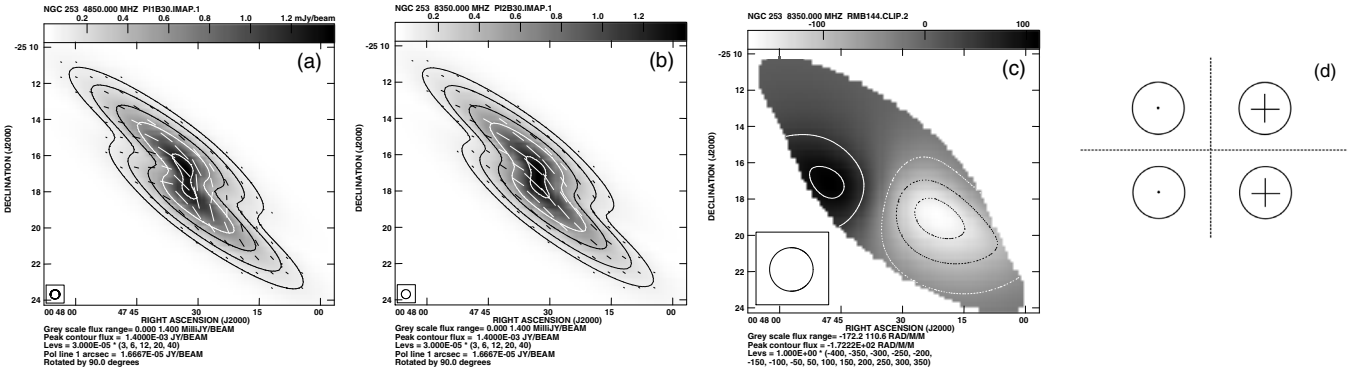


Fig. A.1. Even disk magnetic field. For Figs. A.1–A.12: **a)** polarized flux density and magnetic field orientation at λ 6.2 cm with 30'' resolution. **b)** likewise but for λ 3.6 cm. **c)** RM distribution between $\lambda\lambda$ 6.2 cm and 3.6 cm with 144'' resolution. **d)** sketch of the magnetic field direction.

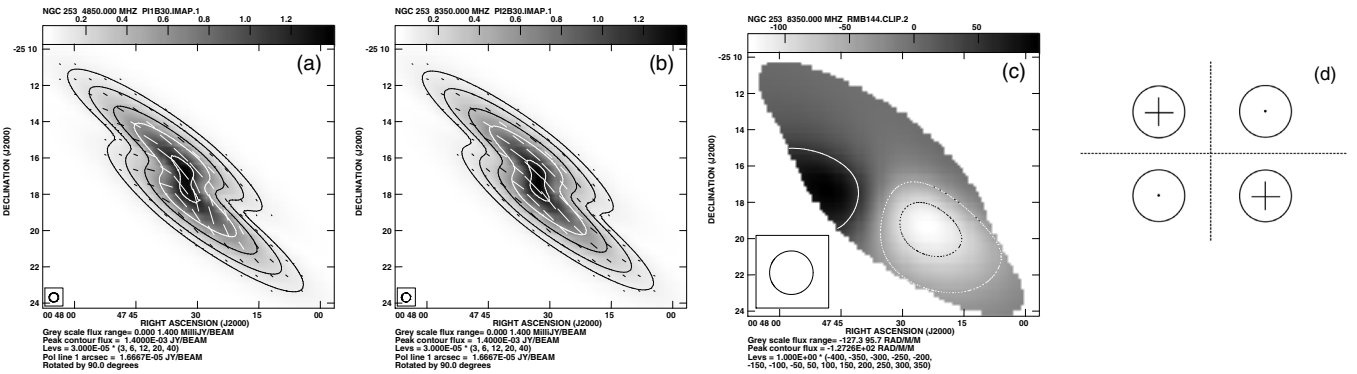


Fig. A.2. Odd disk magnetic field.

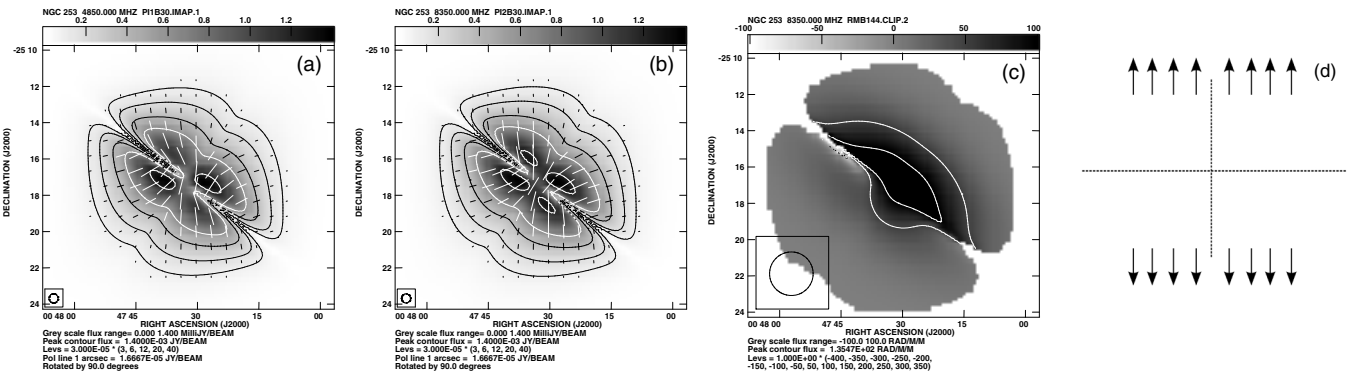


Fig. A.3. Even halo magnetic field. The halo field points away from the disk.

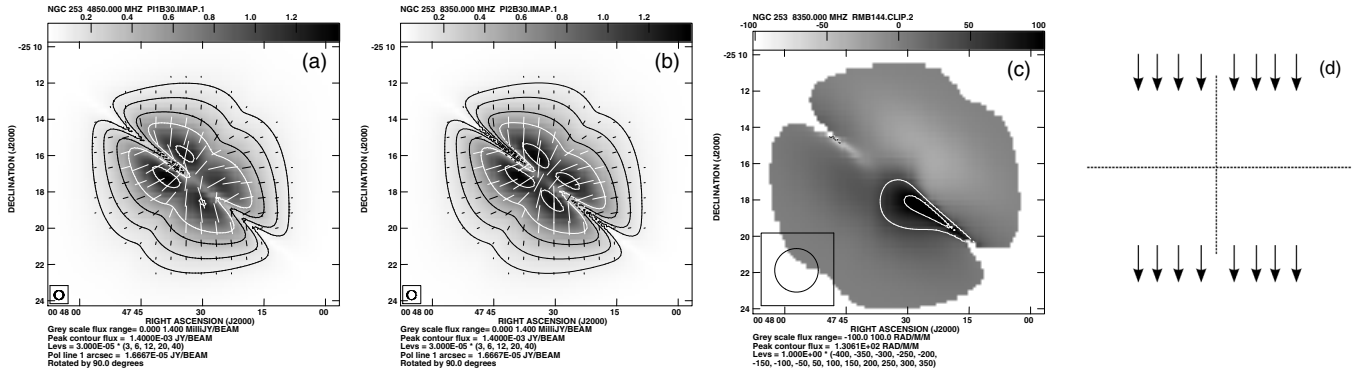


Fig. A.4. Odd halo magnetic field. The halo field points away from the disk in the southern halo.

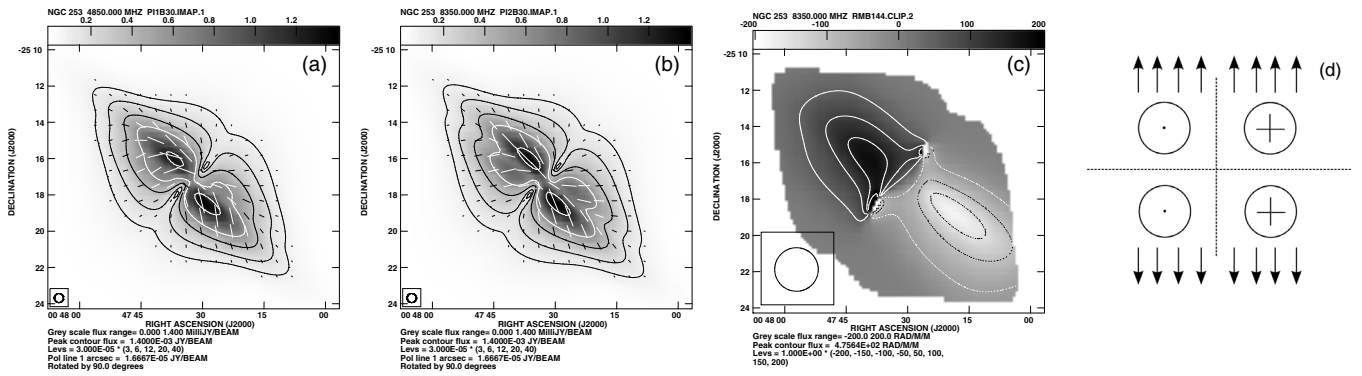


Fig. A.5. Even disk magnetic field and even halo magnetic field. The halo field points away from the disk.

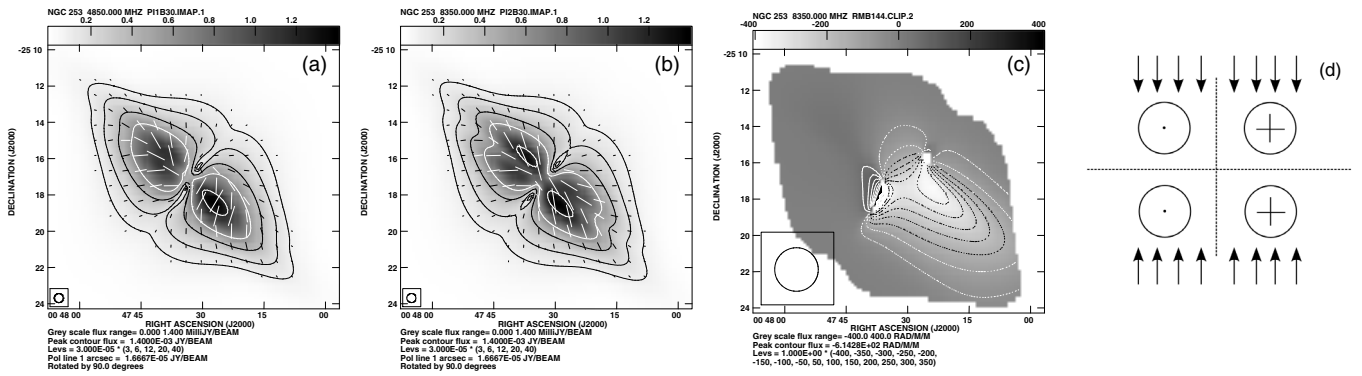


Fig. A.6. Even disk magnetic field and even halo magnetic field. The halo field points towards the disk.

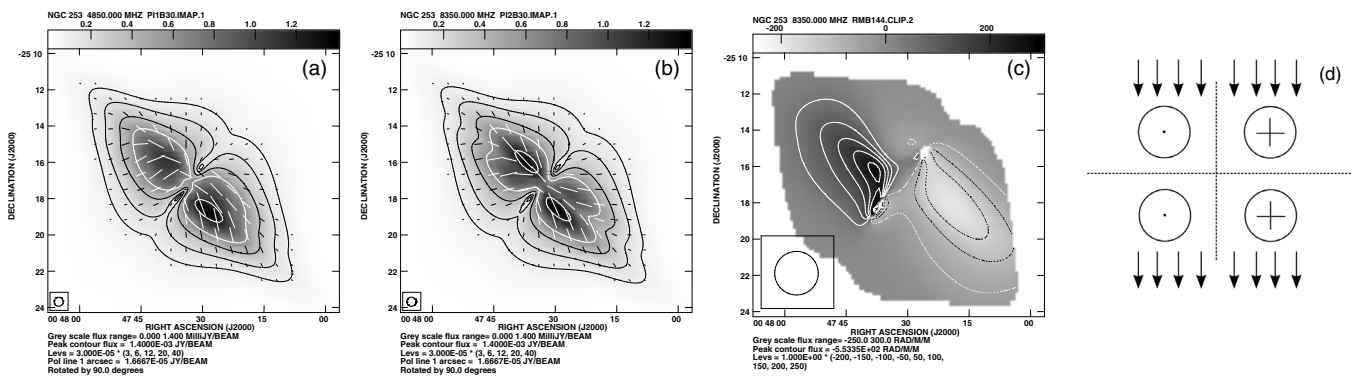


Fig. A.7. Even disk magnetic field and odd halo magnetic field. The halo field points away from the disk in the southern halo.

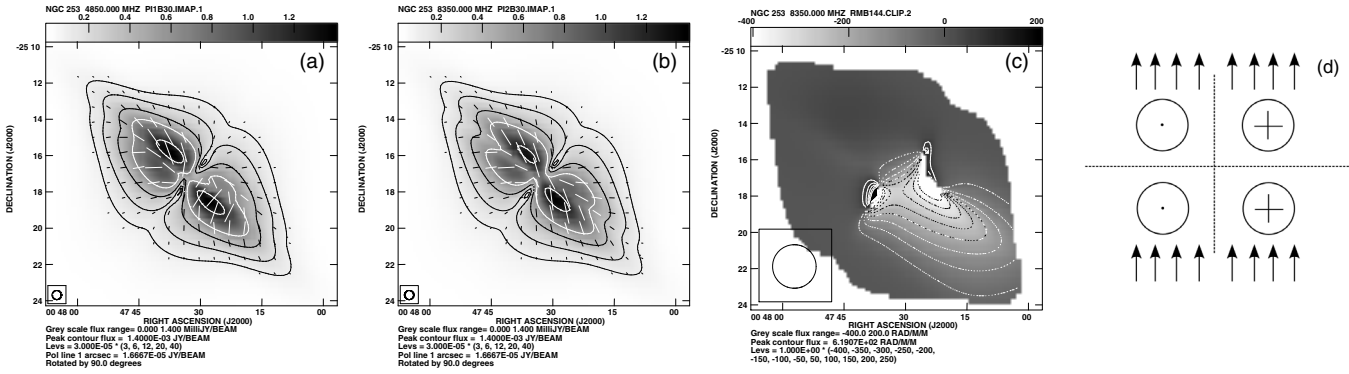


Fig. A.8. Even disk magnetic field and odd halo magnetic field. The halo field points towards the disk in the southern halo.

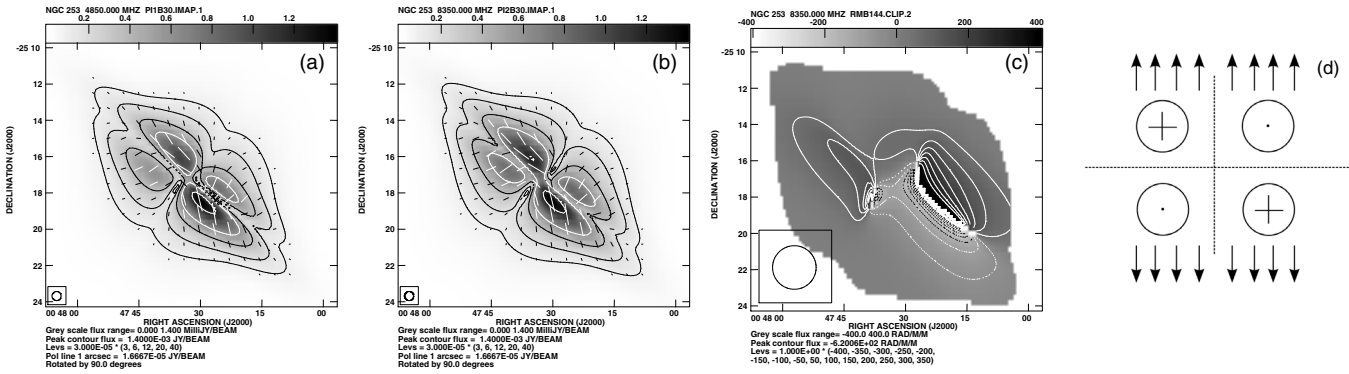


Fig. A.9. Odd disk magnetic field and even halo magnetic field. The halo field points away from the disk.

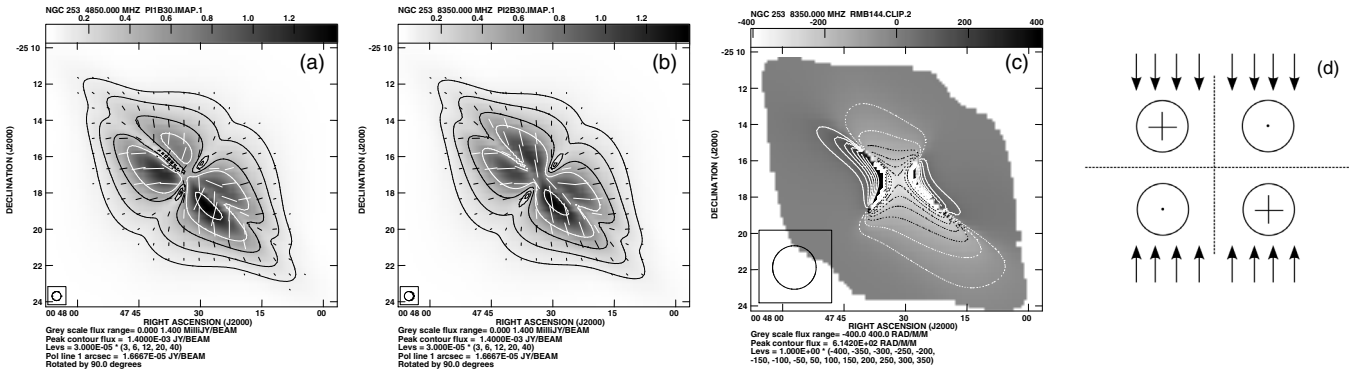


Fig. A.10. Odd disk magnetic field and even halo magnetic field. The halo field points towards the disk.

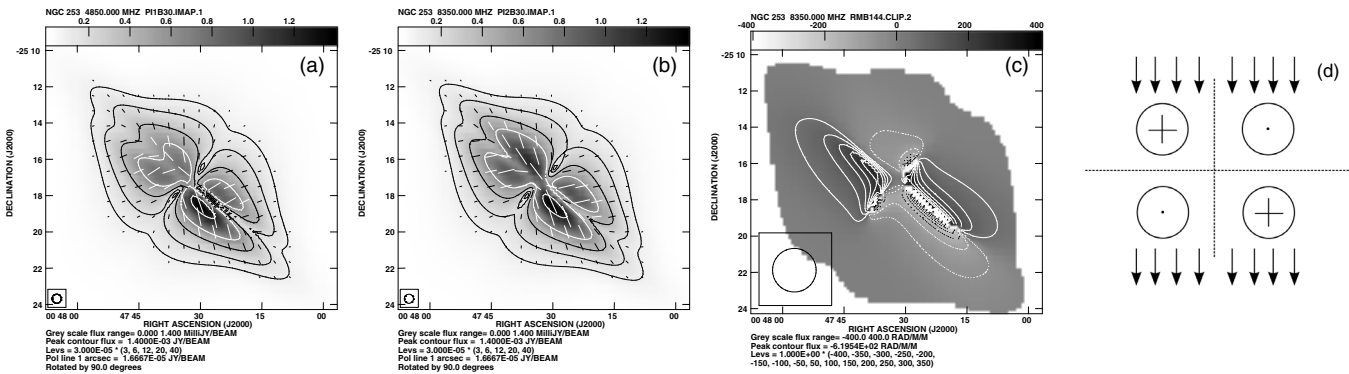


Fig. A.11. Odd disk magnetic field and odd halo magnetic field. The halo field points away from the disk in the southern halo.

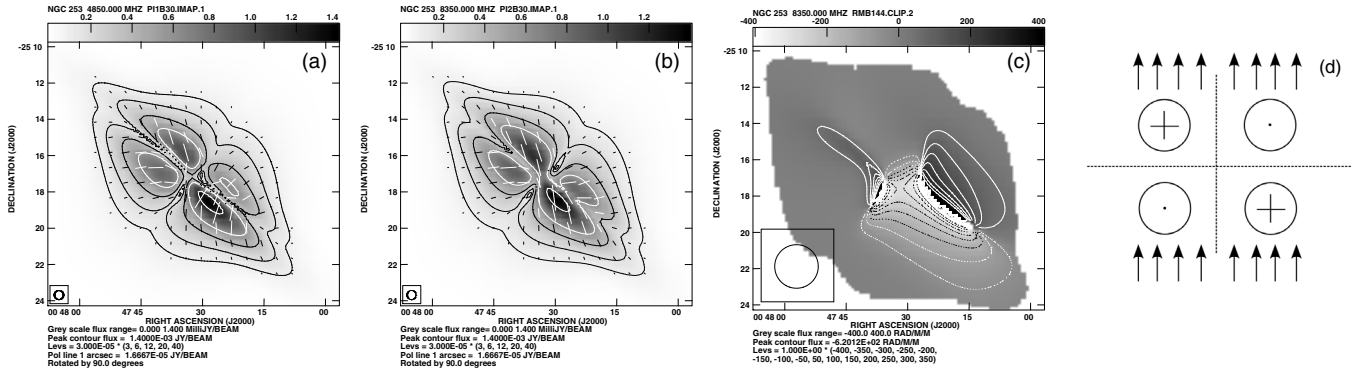


Fig. A.12. Odd disk magnetic field and odd halo magnetic field. The halo field points towards the disk in the southern halo.